THE ASTROPHYSICAL JOURNAL, 563:768–792, 2001 December 20

MEASUREMENT OF THE SECONDARY RADIONUCLIDES ^{10}Be, ^{26}Al, ^{36}Cl, ^{54}Mn, AND ^{14}C AND IMPLICATIONS FOR THE GALACTIC COSMIC-RAY AGE

N. E. YANASAK[1] AND M. E. WIEDENBECK
Jet Propulsion Laboratory, California Institute of Technology, Pasadena, CA 91109
R. A. MEWALDT, A. J. DAVIS, A. C. CUMMINGS, J. S. GEORGE, R. A. LESKE, AND E. C. STONE
California Institute of Technology, Pasadena, CA 91125
E. R. CHRISTIAN AND T. T. VON ROSENVINGE
NASA Goddard Space Flight Center, Greenbelt, MD 20771
AND
W. R. BINNS, P. L. HINK, AND M. H. ISRAEL
Washington University, St. Louis, MO 63130
Received 2000 October 6; accepted 2001 August 2

ABSTRACT

We report on abundance measurements of ^{10}Be, ^{26}Al, ^{36}Cl, and ^{54}Mn in the Galactic cosmic rays (GCRs) using the Cosmic-Ray Isotope Spectrometer (CRIS) instrument aboard the *Advanced Composition Explorer* spacecraft at energies from $\sim$70 to $\sim$400 MeV nucleon^{-1}. We also report an upper limit on the abundance of GCR ^{14}C. The high statistical significance of these measurements allows the energy dependence of their relative abundances to be studied. A steady-state, leaky-box propagation model, incorporating observations of the local interstellar medium (ISM) composition and density and recent partial fragmentation cross section measurements, is used to interpret these abundances. Using this model, the individual galactic confinement times derived using data for each species are consistent with a unique confinement time value of $\tau_{esc} = 15.0 \pm 1.6$ Myr. The CRIS abundance measurements are consistent with propagation through an average ISM hydrogen number density $n_H = 0.34 \pm 0.04$ H atoms cm^{-3}. The surviving fractions, f, for each radioactive species have been calculated. From predictions of the diffusion models of Ptuskin & Soutoul, the values of f indicate an interstellar cosmic-ray diffusion coefficient of $D = (3.5 \pm 2.0) \times 10^{28}$ cm^2 s^{-1}.

Subject headings: cosmic rays — Galaxy: general — Galaxy: halo — ISM: abundances

1. INTRODUCTION

The composition of the galactic cosmic rays (GCRs) observed in the vicinity of Earth results from a source composition that has been transformed by physical processes during transport. Consequently, the study of GCR composition concerns the details of cosmic-ray transport as well as the nature of the GCR source. During transport, cosmic-ray particles diffuse through the Galaxy, traveling through regions of varied matter density, magnetic field strength, and fractional ionization of the interstellar medium (ISM) and ultimately escaping the Galaxy or becoming thermalized in the ISM. They may undergo spallation in the ISM, transforming a parent nucleus into lighter, daughter nuclei. Radioactive species with half-lives smaller than the time of GCR confinement in the Galaxy may experience decay in flight. The steady-state abundances of these species will depend on the amount injected by the source, if any, and the balance between the production rate from spallation in the ISM and loss rates from Galactic escape, decay, or nuclear interactions during transport.

Secondary GCRs are those produced by fragmentation during transport of the primary GCRs, which are present at the source, and fragmentation of other secondaries. Abundances of the stable secondaries indicate the average amount of ISM material traversed during GCR propagation before escape. Because secondary radioactive cosmic-ray species will be created and decay only during transport, their steady-state abundances will be sensitive to the confinement time if their mean lifetimes are comparable to or shorter in duration than this time (see Simpson & Garcia-Munoz 1988 and references therein). Species with significantly longer lifetimes than the GCR confinement time will behave as if they were stable species; those with lifetimes that are significantly shorter will be sensitive to the confinement time, but their GCR abundances will be small. Using experimental measurements of secondary-to-primary ratios such as B/C to determine the average amount of ISM material traversed, the cosmic-ray confinement time can be derived using the abundance of long-lived β-decay secondary radionuclides (for a recent review of GCR secondary radionuclide "clock" studies, see Ptuskin & Soutoul 1998b). Because the fractional abundance that survives transport for these species depends on the loss rate by fragmentation in the ISM, the ISM density in a region traversed by a radioactive species during its lifetime can also be studied.

The abundance of the clock isotope ^{10}Be in the cosmic rays was first deduced from satellite measurements aboard the *Interplanetary Monitoring Platform* (*IMP*) *7* and *8* spacecraft (Garcia-Munoz, Mason, & Simpson 1975) about 25 years ago, contemporaneously with pioneering attempts using balloon-borne instruments (e.g., Webber et al. 1977; Hagen, Fisher, & Ormes 1977; Buffington, Orth, & Mast 1978). The *ISEE 3* spacecraft was the first cosmic-ray experiment to achieve separation of the ^{10}Be abundance peak in a histogram of measured particle masses (Wiedenbeck & Greiner 1980). These earlier measurements were interpreted using a simple "leaky-box" model (LBM),

[1] Now at Human Neuroimaging Facility, Department of Psychology, University of Georgia, Athens, GA 30602; yanasak@arches.uga.edu.

which replaces the spatial diffusion and loss of particles at the boundary of the Galaxy by a phenomenological mean path length through the ISM for escape, which has no spatial dependence. This mean path length, λ_{esc}, determined from secondary-to-primary ratios as stated before, is related to the mean ISM density traversed by the GCRs and the mean confinement time in this model by the expression $\tau_{esc} = \lambda_{esc}/\mathscr{M} n_{ISM} \beta c$. Here, βc is the GCR velocity in the ISM, τ_{esc} is the confinement time, n_{ISM} is the mean ISM number density, and $\mathscr{M}$ is the mean atomic weight of the ISM material. In practice, some groups choose to report the mean ISM hydrogen number density n_H instead of the mean ISM number density, which can be translated into a mean ISM density by knowing the H/He ratio used by each group. In the context of the leaky-box model, the mean properties of the ISM referred to are averaged within the GCR propagation volume around the Earth, not necessarily within the whole Galaxy. The balloon measurements suggested a mean ISM number density ranging from $\sim$0.23–0.70 atoms cm^{-3}, while the abundances reported from the *IMP 7* and *8* and *ISEE 3* spacecraft were more consistent with a narrower range of densities at the lower end of the balloon measurement range $n_{ISM} \sim 0.2$–0.33 atoms cm^{-3} and a confinement time of $\sim$8–20 Myr. These observations led to the initial conclusion that the mean density in the confinement volume is less than the mean density in the Galactic disk, which was taken to be $\sim$1 atom cm^{-3} (e.g., Garcia-Munoz et al. 1975).

The confinement time and mean ISM density can be determined using radioactive species other than ^{10}Be as well. Secondary radionuclides observed at Earth originate within a volume surrounding the solar system having a radius proportional to the diffusion length, l, during their mean lifetime τ_{decay}. This length is given as

$$l = (D\gamma\tau_{decay})^{1/2} , \quad (1)$$

where D is the interstellar diffusion coefficient and γ is the Lorentz factor. Therefore, one can potentially probe the average ISM density within volumes of different radii around the solar system using clock species with different half-lives. One can also investigate whether different radionuclides have the same confinement volume, which would be expected if the primary parents came from the same spatial source distribution. Table 1 shows a list of species with half-lives suitable for this study. In addition to improved abundance measurements of ^{10}Be, measurements of ^{26}Al, ^{36}Cl, and ^{54}Mn have been made by experiments on the *ISEE 3* (Wiedenbeck 1983) and *Voyager* spacecraft (Lukasiak, McDonald, & Webber 1994b, 1997a) and with greatly improved resolution by the experiment on the *Ulysses* spacecraft (Connell 1998; Connell, DuVernois, & Simpson 1998; Simpson & Connell 1998; DuVernois 1997). Interpretation of these abundances using an LBM reveals a similar propagation history among all species, with the mean ISM number density $n_{ISM} \simeq 0.19$–0.52 atoms cm^{-3} and $\tau_{esc} \simeq 9$–27 Myr.

The absence of gross differences in the ISM densities and confinement times inferred from the different radionuclides is not necessarily surprising, considering that the range in half-lives is limited. Secondary species with shorter decay lifetimes such as ^{14}C, with a half-life $\sim$300 times shorter than the half-life of ^{10}Be, can be used to probe the very local ISM density. One can sample a larger neighborhood in the Galaxy by measuring abundances for the secondary radioactive species at higher energies, where relativistic time dilation increases the decay lifetime. Preliminary attempts to measure ^{10}Be at higher energies with balloon instruments generally lacked the statistics and mass resolution to show significant differences from satellite measurements (e.g., Buffington et al. 1978). Measurements from the SMILI experiment (Ahlen et al. 2000) have led to ISM density predictions that are unexpectedly higher ($\gtrsim$1 atom cm^{-3}) than those from low-energy data, although the statistics for this experiment are low (nine ^{10}Be events). A more recent, direct measurement of the ^{10}Be isotopic abundance was made by the balloon-borne ISOMAX experiment (Streitmatter et al. 1993) during its 1998 flight, and a preliminary analysis of the data ($E \sim 0.4$–1 GeV nucleon^{-1}) indicates an ISM density consistent with lower energy satellite data (Geier 2000), albeit with a large uncertainty [$\sigma(^{10}\text{Be}/^{9}\text{Be}) \sim 40\%$]. In addition, attempts have been made to investigate the behavior of radionuclides using measurements of elemental ratios that involve the abundances of the radioactive parent and its daughter product (e.g., Webber et al. 1998a), but this type of analysis is problematic. Because isotopic species are not identified using this method, one cannot uniquely demonstrate that a measured change in the relative elemental abundances with increasing energy results from an increase in the radioactive isotope abundance or from a deviation in the measured abundances of the other stable isotopes from theoretical predictions. Energy dependences could also arise from uncertainties in transport model input parameters (e.g., fragmentation cross sections) or from new physical phenomena.

In this paper, we report new measurements of ^{10}Be, ^{26}Al, ^{36}Cl, and ^{54}Mn at energies from $\sim$70 to $\sim$400 MeV nucleon^{-1} made using the Cosmic Ray Isotope Spectrometer (CRIS) instrument aboard the *Advanced Composition Explorer* (*ACE*) spacecraft (Stone et al. 1998a). We compare the isotopic abundances measured using *ACE*/CRIS to results from previous experiments, and we report an upper limit on the abundance of the rare GCR isotope ^{14}C. From the abundances of stable secondaries measured using CRIS, we determine the mean path length responsible for the production of the clock isotopes. We compare our clock abun-

TABLE 1

DECAY HALF-LIVES OF SECONDARY RADIONUCLIDES

Clock Isotope	Decay Mode	Mode Half-Life	Reference
^{10}Be.....	β^-	1.51×10^6 yr	1
^{14}C.....	β^-	5700 yr	2
^{26}Al[a]	β^+	8.73×10^5 yr	3
	e-capture	8.45×10^6 yr	3
^{36}Cl[a]	β^-	3.07×10^5 yr	2
	e-capture	1.59×10^7 yr	2
^{54}Mn[b]	β^-	$(6.3 \pm 1.7) \times 10^5$ yr	4
	β^-	$(9.3 \pm 3.9) \times 10^5$ yr	5
	e-capture	312 days	6

[a] Although these species decay by *e*-capture as well as by β-decay, the *e*-capture mode is negligible for these species (see § 4).

[b] The species ^{54}Mn also decays by β^+. However, the half-life for this decay is much longer ($\sim$500 times) than the β^--mode half-life, so the β^+-decay mode is negligible.

REFERENCES.—(1) Ajzenberg-Selove 1988. (2) Be, Coursol, & Duchemin 1999. (3) Endt 1990. (4) Wuosmaa et al. 1998. (5) Zaerpoor et al. 1997, 1999. (6) Firestone 1996. Data from (1), (2), and (3) were extracted using the NNDC On-Line Data Service from the ENSDF database, using revisions 1999 February, 2000 July, and 2000 January, respectively.

dance measurements to predictions from a simple LBM model to find values for the confinement time and mean ISM density indicated by each species, in an attempt to provide a consistent picture of GCR propagation for all the secondary radionuclides. Taking advantage of the high statistical significance of the CRIS data set, we present measurements for the abundances of these species at multiple energies for comparison with the expected energy dependence from this model.

Because leaky-box models assume a homogeneous ISM matter distribution, observable differences arise in the predictions between the LBM and more realistic models of GCR propagation (e.g., Ptuskin & Soutoul 1998a; Strong & Moskalenko 1998) for the different clock isotopes if significant inhomogeneities in the matter distribution exist. In addition, the models that may incorporate diffusion, convection, and reacceleration of the GCRs as they propagate through an inhomogeneous Galactic matter distribution make predictions using the GCR clock surviving fraction for quantities that have more direct astrophysical significance such as the scale height of the Galactic halo or the Galactic diffusion coefficient. We discuss implications of our data for these models of GCR transport in addition to the LBM. Finally, we consider uncertainties in modeling GCR transport in general (see Appendix A) and discuss their effect on the interpretation of our measurements and of previously reported results.

2. OBSERVATIONS

The *ACE*/CRIS instrument (Stone et al. 1998a), used to obtain the data reported here, measures the GCR elemental and isotopic composition by using multiple measurements of dE/dx versus total energy (Goulding & Harvey 1975). CRIS consists of four stacks of large-area Li-drifted Si detectors 10 cm in diameter with nominal thicknesses of 3 mm that measure energy loss of the particles (total instrument geometry factor ~ 250 cm^2 sr). Trajectories are determined using a scintillating optical fiber trajectory hodoscope (SOFT) above the Si stacks. The SOFT system consists of three pairs of x-y planes, with an active dimension of 26 cm $\times$ 26 cm, constructed out of 200 $\times$ 200 μm square cross section scintillating fibers and an additional pair of fiber planes at the top of the instrument that serve as a trigger. Light output from the fibers is routed to a CCD camera.

The period of observation for these data extends from 1997 August 27 to 1999 April 9 for ^{10}Be, ^{26}Al, ^{36}Cl, and ^{54}Mn. The period for ^{14}C is slightly longer to improve the statistics for this very rare isotope (1997 August 27 to 1999 July 8). Days of significant solar energetic particle intensity were excluded from these periods as well as days during which the spacecraft was inserted into its orbit. The remaining period of active data collection is 401 days for ^{10}Be, ^{26}Al, ^{36}Cl, and ^{54}Mn, and 442 days for ^{14}C.

Events were selected for this study to avoid contamination from the small number of particles with large uncertainties in their identification, which result from sources such as observation of multiple particles within the resolving time of the electronics. After event selection, corrections in the abundances were made to account for selection criteria that could affect the relative isotopic abundances. Nuclei selected for this study were required to enter into the detector through the SOFT hodoscope at the top of the instrument. Those penetrating less than 0.6 cm from any edge of the trigger plane in SOFT were eliminated. Particle trajectories for which the three coordinate pairs from the hodoscope did not lie within 5 standard deviations of a straight line (the measured standard deviation for SOFT ~ 100 μm) were rejected.

In addition to trajectory uncertainties introduced by the hodoscope, uncertainties in the response of the Si detectors to particle events can occasionally lead to misidentification. The CRIS Si detectors have surface "dead layers," which are not negligible ($\sim 2\%$ of the nominal detector thickness), within which deposited particle energy will not fully contribute to the measured pulse height. Nuclei stopping close to the dead layers were rejected from this study to avoid misidentification from the incomplete registration of the deposited energy. Background events in which the incident particle fragmented in the Si stack or exited through the sides or in which multiple particles traversed the detector within the time resolution of CRIS were eliminated by demanding consistency among multiple charge and mass determinations. Using different detector combinations to measure the residual energy of a stopping particle, E', near the end of range and the upstream energy loss, ΔE (the "$\Delta E - E'$ technique," described in Stone et al. 1998b), three charge determinations were obtained for each particle event. Given two different charge determinations $Z1$ and $Z2$, a charge consistency parameter $(Z2 - Z1)/Z1$ can be defined, as shown in Figure 1. From the three charge determinations mentioned above, two different charge consistency parameters were defined, and the mean and standard deviation for the distribution of each charge consistency parameter were determined, using the CRIS data set before event selection. Events differing by more than 5 standard deviations from the mean of each distribution were rejected.

Between two and seven mass determinations were obtained in a similar manner to the charge determinations using an individual detector to measure ΔE in each case, with the number of determinations depending on the number of Si detectors penetrated before stopping of the particle. Given a particular detector combination, the mean and standard deviations for mass distributions of a particular charge species were determined as well. The mass for each event was calculated from a χ^2 fit of the mass determinations from each detector combination using the corresponding means and standard deviations. Particles having a χ^2 value lying above a cutoff indicating a 94% statistical probability for an event to have a χ^2 of equal or lower value were eliminated.

A full Monte Carlo simulation of the instrument was performed as well as an analytical treatment of the instrument charge and mass resolution during the instrument design. Mass resolution in the CRIS instrument is limited by the effects of Landau fluctuations in energy deposited in the Si telescopes and multiple Coulomb scattering. As shown in Stone et al. (1998a), the mass resolution is dependent on the charge of the cosmic-ray species. The mass resolution also degrades with an increase in the "zenith" angle theta, defined as the incidence angle of the particle trajectory with respect to a normal to the detector surface (Stone et al. 1998a). For example, the mass resolution for ^{56}Fe is $\sigma_M \simeq 0.23$ amu at $\theta \leq 10°$, which increases to $\sigma_M \simeq 0.32$ amu at $\theta \leq 40°$. For $\theta \leq 30°$, the mass resolution varies from $\sigma_M \simeq 0.13$ to 0.27 amu in the charge range $Z = 6$–26. This resolution is consistent with expectations from the instrument simulation (Stone et al. 1998a). For this study, a

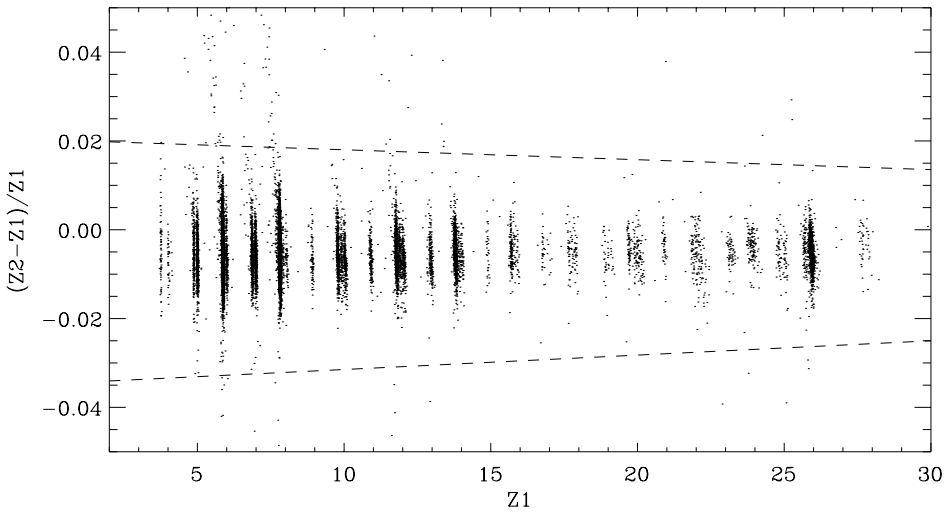

FIG. 1.—Charge consistency measure vs. charge. Each determination of charge uses a different combination of detectors to measure the residual energy of a stopping particle, E', near the end of range and the upstream energy loss, ΔE. In this example, $Z1$ was calculated using the energy deposited in the Si detector that stopped the particle for E' and the energy deposited in all previous upstream detectors as ΔE. The charge $Z2$ was determined using the energy deposited in the Si detector at the top of the stack as ΔE and all subsequent downstream detectors as E'. The dashed lines on the plot correspond to 5 standard deviations from the mean value of $(Z2 - Z1)/Z1$ for a particular charge. A subset ($\sim$18,000) of all events in the CRIS data are plotted.

cutoff zenith angle was chosen for each species to minimize the overlap between peaks in the mass distributions and maximize the statistical sample, and these angles are shown in Table 2.

Mass histograms for the GCR elements Be, Al, Cl, and Mn containing secondary radionuclides are shown in Figure 2, and the C histogram is shown in Figure 3. The statistics of the CRIS data set also allow measurement of the isotopic abundances for the clock isotopes at multiple energies; the mass histograms for several energy intervals are shown in Figure 4. After the selection of events with an unambiguous mass identification using criteria mentioned above, the peak shapes are approximately Gaussian. The isotopes of Be, Al, Cl, and Mn have clearly resolved peaks in the histograms and, with the exception of Mn, there is very little overlap between adjacent mass peaks. The major carbon isotopes, ^{12}C and ^{13}C, are also well-resolved, demonstrating the potential for good resolution of ^{14}C from shoulders in the ^{13}C mass peak if ^{14}C were present.

With the exception of Be and C, the isotopic abundances were determined using the maximum-likelihood method to fit Gaussian peak shapes to the histograms, and these fits are shown overlying the histograms. Because of the excellent mass separation for lighter elements, the Be isotopic

TABLE 2

ABUNDANCES OF THE GALACTIC COSMIC-RAY RADIONUCLIDES NEAR EARTH

Ratio	Energy (MeV nucleon^{-1})	Typical ISM Energy[a] (MeV nucleon^{-1})	Maximum Angle (deg)	rms Mass (amu)	Measurement[b]
^{10}Be/^{9}Be	70–145	120–350	40	0.09	0.120 ± 0.008
	E1: 70–95				0.123 ± 0.013
	E2: 95–120				0.115 ± 0.013
	E3: 120–145				0.122 ± 0.016
	SIS:[c] 20–70				0.147 ± 0.036
^{14}C/C	70–210	120–430	15	0.10	$<2.3 \times 10^{-4}$[d]
^{26}Al/^{27}Al	125–300	190–560	40	0.17	0.042 ± 0.002
	E1: 125–183				0.042 ± 0.003
	E2: 183–242				0.043 ± 0.004
	E3: 242–300				0.037 ± 0.004
^{36}Cl/Cl.....	150–350	210–580	30	0.19	0.061 ± 0.007
	E1: 150–250				0.056 ± 0.010
	E2: 250–350				0.063 ± 0.011
^{54}Mn/Mn.....	178–400	240–630	30	0.24	0.109 ± 0.006
	E1: 178–252				0.113 ± 0.010
	E2: 252–326				0.109 ± 0.011
	E3: 326–400				0.106 ± 0.012

[a] Approximately 95% of the GCRs observed by CRIS within the energy range shown in the second column have typical ISM energies shown in the third column. The ISM energies were calculated using a model by Fisk 1971, described in § 3.

[b] These relative abundances include corrections for differences in geometry factors, detection efficiency, and nuclear fragmentation within the instrument. Uncertainties reflect 1 standard deviation statistical uncertainties only.

[c] This lowest energy point was measured using the SIS instrument aboard the *ACE* spacecraft.

[d] Eighty-four percent confidence level on the upper limit.

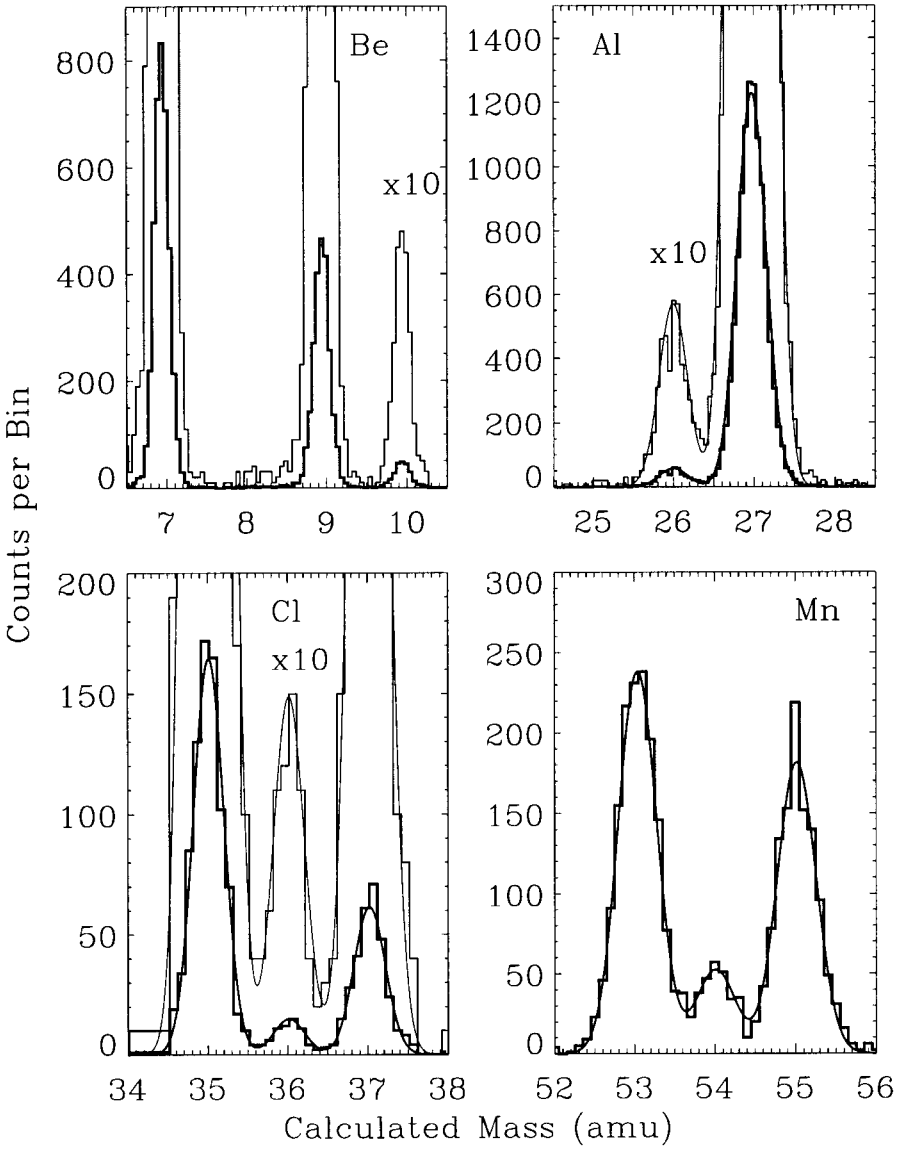

FIG. 2.—Mass histograms for Be ($\langle E\rangle = 107$ MeV nucleon^{-1}), Al ($\langle E\rangle = 212$ MeV nucleon^{-1}), Cl ($\langle E\rangle = 250$ MeV nucleon^{-1}), and Mn ($\langle E\rangle = 289$ MeV nucleon^{-1}). The maximum allowed zenith angles for these data are $\theta_{max} < 40°$ for Be and Al and $\theta_{max} < 30°$ for Cl and Mn. The overlying curves for Al, Cl, and Mn were obtained using maximum-likelihood fits, as discussed in the text. A 10× magnification of the Be, Al, and Cl counts scale is shown as a light histogram and fitted curve. The total number of events in the histograms are 6552 for Be, 10967 for Al, 1196 for Cl, and 2954 for Mn.

abundances were obtained by counting events in each peak. Small corrections to the measured relative abundances (<12% for the Be isotopes, <4% for all others) were made to take into account isotopic differences in fragmentation in the instrument, SOFT efficiency, and geometry factor for a given energy bin. The resulting isotopic abundance ratios, after application of these corrections, are shown in Table 2.

After calculating the isotopic abundances using fits to peaks in the mass histograms, an adjustment must be made to account for the small amount of background contribution to the secondary radionuclide abundances. This background is most likely due to two sources: spillover from adjacent isotopes due to non-Gaussian tails and fragmentation in the material at the top of CRIS. For example, the charge consistency criteria and multiple mass determinations described above will most likely not eliminate a GCR particle that loses a neutron in the ~ 0.442 g cm^{-2} above the Si detectors. Mass histograms for some of the more abundant elements in GCRs show evidence of small mass peaks for radioactive species that are not present in the GCRs because of their short half-lives (e.g., ^{22}Na, which decays by β^+-emission in $\tau_{1/2} = 2.6$ yr). An estimate of the overall background contribution was made in the following manner. Using elements that are abundant in the GCRs such as carbon and silicon, mass histograms were generated, and the abundance of the lightest stable GCR isotope in each histogram was determined. Events in the mass region below this peak, which should be only background, were counted if they were within 3 standard deviations of 1 amu below the peak. Using this sum of background event counts, the amount of background to be subtracted was calculated as a percentage of the abundance for the lightest stable isotope. A value of this percentage averaged over all of the abundant GCR species was calculated and an uncertainty was assigned to bound the range of percentages. The amount of background subtraction applied to the secondary radionuclide species was $0.7^{+0.7}_{-0.5}$% of the adjacent, heavier peak. This adjustment is negligible for ^{10}Be, but the

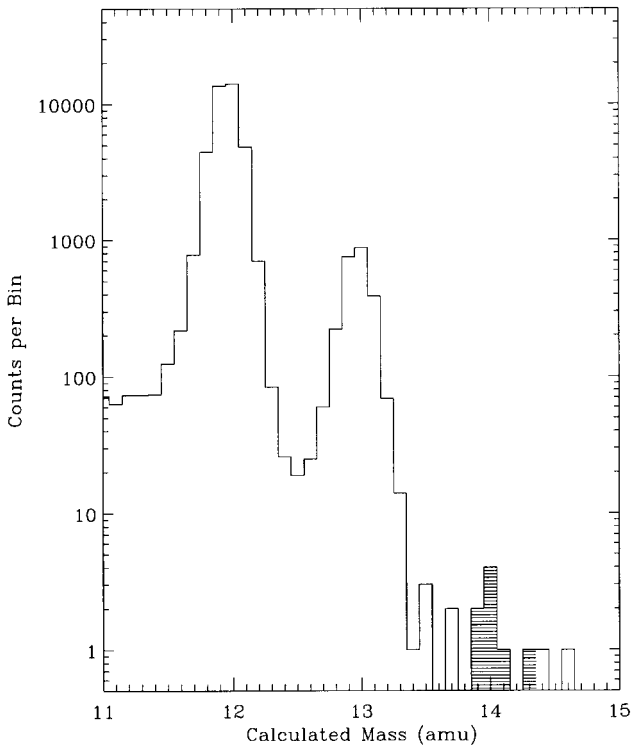

FIG. 3.—Log scale mass histogram for C ($\langle E \rangle = 134$ MeV nucleon^{-1}). Maximum allowed zenith angle for these data is $\theta_{max} < 15°$. The hatched region shows the data that fall within 3 standard deviations of the ^{14}C central peak mass located at 14 amu. One standard deviation is 0.10 amu, from a maximum-likelihood fit of a Gaussian shape to the ^{12}C peak. This data set contains 41,805 C events.

amount of adjustment to the ^{26}Al/^{27}Al, ^{36}Cl/Cl, and ^{54}Mn/Mn ratios was ~14%, ~3%, and ~2%, respectively. The results in Table 2 include these corrections.

A limit on the abundance of ^{14}C was calculated in the following manner. From fitting the ^{12}C peak, the standard deviation of the mass distribution of events was determined to be $\sigma = 0.10$ amu. Events within 3 standard deviations of the ^{14}C central peak mass located at 14 amu were counted and included in the ^{14}C abundance. Measuring the abundance of GCR ^{14}C is complicated by contamination due to a small amount of ^{14}C produced via fragmentation of heavier GCR nuclei interacting in the instrument. Most of the observed ^{14}C abundance probably resulted from fragmentation in the upper parts of the instrument or from spillover from neighboring abundance peaks, so the measured abundance corresponds to an upper limit for the GCR ^{14}C. Estimating the amount of ^{14}C from sources other than the natural GCR abundance requires a fairly detailed model of detector response to account for the fraction of interaction products not eliminated by charge- and mass-consistency cuts. However, we can compare the observed amount of ^{14}C with trace abundances measured with CRIS for short-lived species, which are produced solely by fragmentation in CRIS or exist because of spillover. Estimates of species such as ^{16}N and ^{12}B measured with CRIS, with half-lives of the order of milliseconds to seconds, indicate that the majority of the observed ^{14}C is not of Galactic origin.

Figure 5 shows a comparison between CRIS abundances for the secondary radionuclides measured at Earth and those obtained previously from *Ulysses* (Connell 1998; Connell et al. 1998; DuVernois 1997; Simpson & Connell 1998), *ISEE 3* (Wiedenbeck & Greiner 1980; Wiedenbeck 1983), *Voyager* (Lukasiak et al. 1994a, 1997a, 1997b), *IMP 7* and *8* (Garcia-Munoz, Simpson, & Wefel 1981), and balloon experiments (Webber & Kish 1979; Webber 1982). Other experiments that report only upper limits on the abundance for these species are not shown for clarity. Previous abundance measurements were made at different levels of solar modulation, and these have been adjusted to the level of modulation appropriate to CRIS for direct comparison (see § 3 for details). Because these adjustments rely on modulation levels determined by each experiment, the comparison is approximate. The largest adjustment required was 25% for the *ISEE 3* measurement of ^{10}Be/^{9}Be (Wiedenbeck & Greiner 1980).

The uncertainties shown in Figure 5 are statistical and do not include instrumental systematics, uncertainties in solar modulation corrections, or uncertainties in the atmospheric corrections for the balloon abundances. The CRIS data are generally consistent with those from previous experiments to within statistical uncertainties. For the ^{10}Be and ^{26}Al clock species, abundance measurements with well-resolved isotopic peaks from experiments other than CRIS exist at different energies, and in theory the energy dependence for these abundances can be tested using these previous measurements. However, several factors complicate this method of probing the energy dependence. One factor is that each previous measurement was generally reported as one abundance per experiment covering a fairly wide energy range, owing to the limited counting statistics. Because most of these previous observations were made with instruments using a similar measurement technique to CRIS, most of the energy ranges covered by previous measurements significantly overlap. Comparisons that used these overlapping measurements tend to deemphasize any subtle abundance variations with energy that may exist. Another complication is that systematic uncertainties in measurements by previous experiments need to be considered. Systematic uncertainties in the analysis of the CRIS data will tend to affect all of the measurements similarly, preserving the energy dependence. The measurement of these abundances from CRIS over different energy bands provides a set of statistically uncorrelated measurements that indicates that there is no statistically significant energy dependence in the clock abundances at these energies.

3. PROPAGATION MODELING

The abundances observed by CRIS were compared with steady-state abundances calculated using a steady-state, leaky-box model (e.g., Meneguzzi, Audouze, & Reeves 1971). Table 3 lists the important parameters of this model, which are described later in this section in greater detail. This model is an approximation to a class of models that simulate the spatial and temporal evolution of GCR particles in the Galaxy during transport, incorporating processes such as diffusion (see § 1). The LBM replaces the Galactic matter distribution with a spatially independent distribution of path lengths through which the GCRs propagate before escape.

Formally, the distribution of path lengths through which GCRs propagate in leaky-box models is exponential (Davis 1960) with a mean value, λ_{esc}, adjusted for agreement with observed GCR abundance data. The mean path length may depend on GCR energy and species, which simulate the

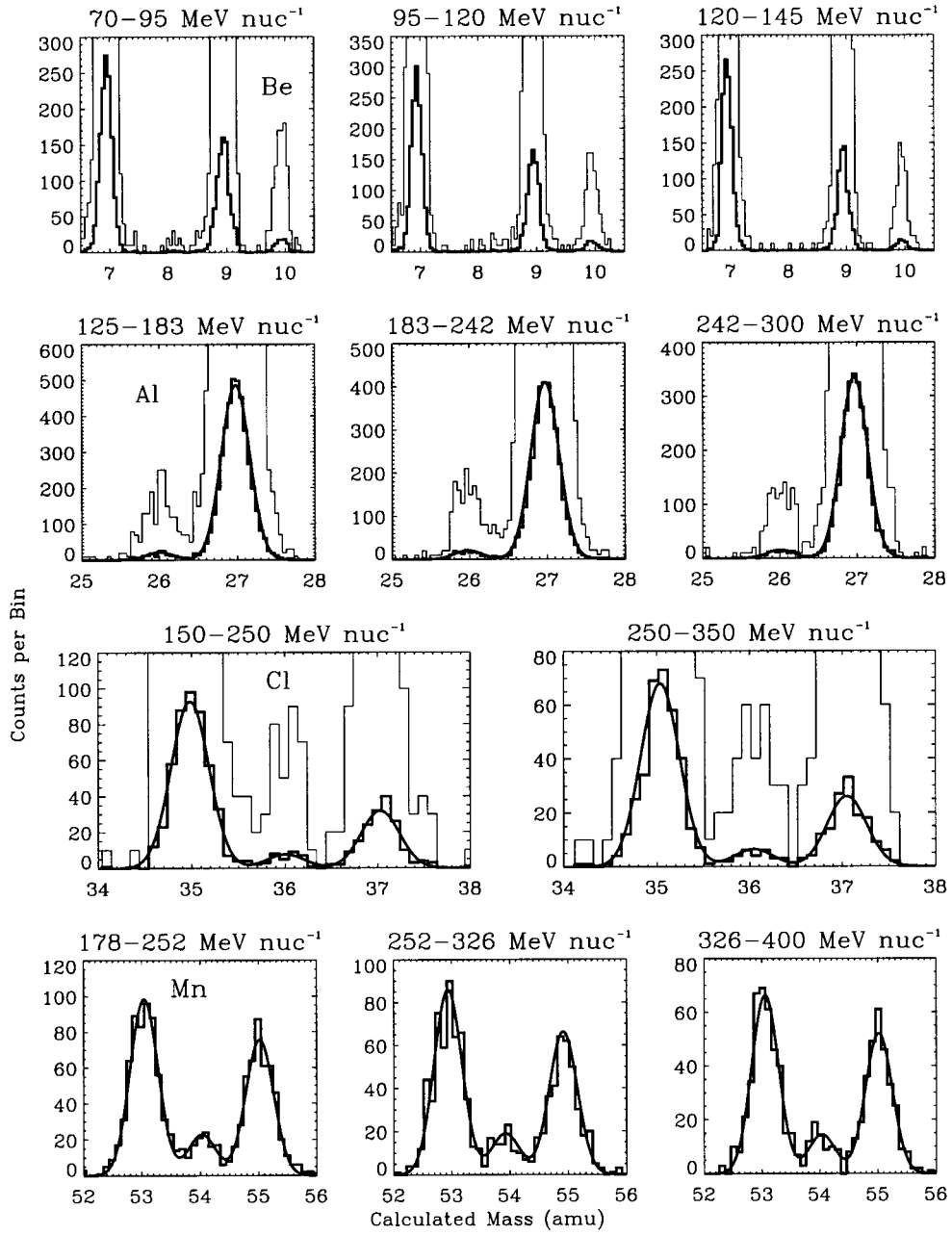

FIG. 4.—Mass histograms for Be, Al, Cl, and Mn measured over different energy intervals reported in Table 2. The energy intervals proceed from lowest to highest moving from left to right across the figure. The maximum allowed zenith angles are the same as in Fig. 2. A 10× magnification of the Be, Al, and Cl abundances is shown as a lighter histogram.

physical dependence of GCR diffusion and Galactic confinement on these quantities. Other path length distributions (PLDs) can be investigated using the "weighted-slab" technique (Fichtel & Reames 1968). Using this technique, the passage of the GCRs through matter and their consequent fragmentation is simulated using slabs of different length, and a distribution of these slab path lengths is specified explicitly to model transport. The weighted-slab technique using an exponential PLD approximates the leaky-box model results with some significant differences (Stephens & Streitmatter 1998). The observed abundances of stable GCR secondaries have been fitted remarkably well using both the weighted-slab technique and steady-state solutions of the leaky-box model, and the mean path length has been found to require an energy dependence to fit the abundances (e.g., Ferrando et al. 1991). The model used in this study, which will be referred to hereafter for simplicity as a "steady-state" model, involves numerical solution of the leaky-box equation as given by Meneguzzi et al. (1971).

The abundances of the secondary clock isotopes measured at Earth correspond to the fraction of the produced abundance that has survived without decaying in transport. The surviving fraction, f, of a GCR secondary radionuclide species i is defined as the ratio of the GCR abundance observed at Earth to the abundance that would be observed if there were no decay in flight. In the LBM, if cosmic-ray energy loss is neglected, the surviving fraction is given by

$$f = \frac{1/\tau_{\rm esc} + 1/\tau_{i,\rm spall}}{1/\tau_{\rm esc} + 1/\tau_{i,\rm spall} + 1/\gamma\tau_{i,\rm decay}} . \quad (2)$$

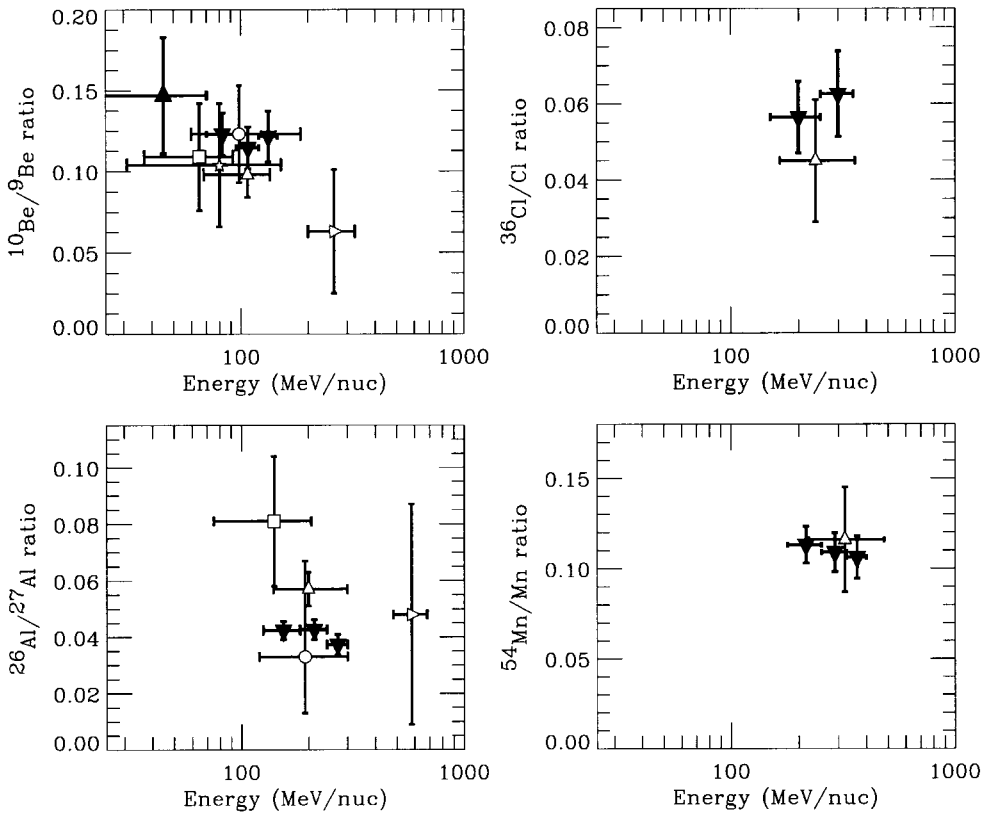

FIG. 5.—Secondary radionuclide abundance ratios from CRIS and previous experiments with a mass resolution of $\sigma_M \leq 0.35$ amu, as a function of energy. Data from CRIS are shown as filled triangles pointing downward. A single data point for the ^{10}Be/^{9}Be ratio using the SIS instrument (Stone et al. 1998b) aboard *ACE* is shown for comparison at lower energy as a filled upward triangle. Ratios for the previous experiments have been adjusted to the level of solar modulation at the time of CRIS observations, $\phi = 325$ MV, for direct comparison. References for the data are as follows: *Circle*, Wiedenbeck & Greiner (1980); Wiedenbeck (1983); *square*, Lukasiak et al. (1994a, 1994b); *open upward triangle*, Connell (1998); Connell et al. (1998); Simpson & Connell (1998); DuVernois (1997); *star*, Garcia-Munoz et al. (1981); *right triangle*, Webber & Kish (1979); Webber (1982); *filled triangles* this study.

In this expression, $\tau_{\rm esc}$ is the GCR confinement time, $\tau_{i,\rm decay}$ is the mean decay lifetime of the radionuclide in its rest frame, $\tau_{i,\rm spall}$ is the characteristic lifetime against spallation in the ISM, and γ is the GCR Lorentz factor. As shown in equation (2), f results from the competition between particle loss by radioactive decay and loss by escape and fragmentation. The value of f depends on the ISM density, $\rho_{\rm ISM}$, as well as on $\tau_{\rm esc}$, since the spallation time, $\tau_{i,\rm spall}$, is proportional to

TABLE 3

PARAMETERS IN THE LEAKY-BOX MODEL

Parameter	Reference	Comments
Source composition:		
Elemental	1	Adjusted to match CRIS observations
Isotopic	2	
Spectra		$dJ/dE \propto p^{-2.35}$, similar to Engelmann et al. 1990
Cross sections:		
Total[a]	3	
Partial[b]	4	
Interstellar Medium:		
Composition	5	90% H, 10% He
Ionization	6	$H^+/H_{\rm tot} = 0.10 \pm 0.04$
Mean path length[c]	7	$\lambda_{\rm esc} = 26.7\beta$ g cm^{-2}/[$(\beta R/1.0\ {\rm GV})^{0.58} + (\beta R/1.4\ {\rm GV})^{-1.4}$]
Solar modulation	8	Equivalent to $\phi = 325$ MV

[a] Energy dependence renormalized to match available cross section data.

[b] See Appendix A. Energy dependence renormalized to match available cross section data.

[c] Form from Soutoul & Ptuskin 1999 adjusted to match CRIS data.

REFERENCES.—(1) Engelmann et al. 1990; DuVernois & Thayer 1996. (2) Anders & Grevesse 1989. (3) Letaw et al. 1983. (4) Silverberg, Tsao, & Barghouty 1998. (5) Peimbert 1975; Churchwell, Mezger, Huchtmeier 1974. (6) Taylor & Cordes 1993; Diplas & Savage 1994; Dame et al. 1987. (7) Soutoul & Ptuskin 1999. (8) Fisk 1971.

$\rho_{\rm ISM}$. In the leaky-box model, the product $\rho_{\rm ISM}\,\tau_{\rm esc}$ is proportional to the mean path length for escape:

$$\lambda_{\rm esc} = \tau_{\rm esc}\,\rho_{\rm ISM}\,\beta c\ . \tag{3}$$

Using $\lambda_{\rm esc}$ inferred from abundance measurements of stable GCR secondaries relative to their primary parents, both $\tau_{\rm esc}$ and $\rho_{\rm ISM}$ can be derived.

Under certain conditions, the LBM appears to be an adequate approximation of diffusion models. For example, a diffusion model of Ptuskin et al. (1997) suggests that low-energy GCRs may move fairly freely (i.e., large diffusion coefficient) within an internal zone encompassing the Galactic disk, which is bounded by another region where hydrodynamic waves are self-generated by the streaming of GCRs. The waves in this bounding region scatter GCRs strongly and efficiently trap them close to the internal zone, effectively simulating a leaky box at low energies within this smaller region of the Galaxy. However, the interpretation of GCR radionuclide data using the leaky-box model may differ from that of diffusion models with inhomogeneous matter distributions, depending on the species and the GCR energy. In an inhomogeneous model, shorter lived secondary radionuclides will tend to be more concentrated around the regions of high ISM density where they are predominantly produced. Density inhomogeneities can be present on a variety of scales ranging from the scale height of the Galactic disk down to the scale of individual molecular clouds. If a medium with large-scale inhomogeneities is involved in the production of the secondary radionuclides that we observe, the abundances for species of different half-lives may not all be simultaneously well represented by an LBM with a single set of input parameters such as average ISM density because they probe different distance scales in the ISM. Thus, the comparison of the different ISM densities derived from the measured abundances of different radionuclides may provide a general insight into the existence and scale of inhomogeneities.

One can also approximate the effects of cosmic-ray transport in the Galaxy by using the weighted-slab technique, which presupposes that the solution can be separated into two parts (e.g., Ptuskin, Jones, & Ormes 1996): a "nuclear part" that dictates the amount of fragmentation for each species in slabs of material of various lengths and an "astrophysical part" that specifies the distribution of these slab path lengths that the GCRs traverse from the source to the Earth. One advantage to this technique is that the path length distribution can be varied from the simple exponential PLD implicit in the LBM. Because particles lose energy during propagation and both the fragmentation cross sections and PLD depend on energy, the separability of the solution is only approximate, and this leads to differences between the predictions of the LBM and the weighted-slab model with exponential PLD (e.g., Stephens & Streitmatter 1998). The weighted-slab technique assumes that the mean path length depends only on the steady-state particle energy (Ptuskin et al. 1996). However, the mean path length used by models that solve the steady-state LBM equations is an average over the energies the GCRs have while slowing down in the ISM, which gives a larger average energy than the steady-state particle energy. In the cosmic-ray energy regime below 1 GeV nucleon^{-1} where ionization energy loss during propagation is a sizable fraction of the initial particle energy, a fit to secondary-to-primary ratio data gives a path length that decreases with decreasing energy (e.g., Garcia-Munoz et al. 1987). This means that the absolute flux at a particular steady-state energy will be underestimated by the weighted-slab technique because the GCRs will traverse a shorter mean path length before escape. Therefore, in the energy regime below 1 GeV nucleon^{-1}, weighted-slab models require a larger mean path length to fit measured secondary-to-primary ratio data at a given energy than steady-state models. Differences in flux predictions for stable secondaries in the two models with an identical mean path length may be as great as 17% (Stephens & Streitmatter 1998).

A difference in predictions between the two models also exists for the secondary radionuclide fluxes, although this difference is somewhat less than that in the predicted stable secondary abundances. Because the ionization energy loss is proportional to Z^2/A, the difference will be greatest for the ^{10}Be clock because of the change from $A/Z \simeq 2.0$ to 2.5 during fragmentation of the parent to create this isotope. At an ISM energy of 250 MeV nucleon^{-1} relevant to CRIS Be data (see Table 2), Stephens & Streitmatter (1998) estimate that the predicted ^{10}Be/^{9}Be abundance ratio in the ISM using a weighted-slab model will be $\sim$2% higher than the LBM ratio. Solar modulation will deemphasize this effect further. However, the mean path length in a weighted-slab model required to match secondary data will be larger, and this will lead to different predictions of $\tau_{\rm esc}$ and the average ISM density for the two models using equation (3).

Abundances at the source for our model were adjusted to match predictions of the propagation model to CRIS data. The elemental abundances are generally consistent within given uncertainties with the elemental source composition derived using *HEAO 3* data (Engelmann et al. 1990) for major elemental species such as C, Si, and Fe and with *Ulysses* observations (DuVernois & Thayer 1996) for rarer elements such as P. Generally, the isotopic abundances are similar to those found in the solar system (Anders & Grevesse 1989) with adjustments for elemental fractionation correlated with first-ionization potential or condensation temperature (e.g., Meyer, Drury, & Ellison 1997; Meyer 1985), with one notable exception being the well-documented source enhancement of ^{22}Ne (e.g., Mewaldt 1988 and references therein; for a recent measurement of ^{22}Ne, see Binns et al. 2000).

Source spectra were assumed to be power laws in momentum $dJ/dE \propto p^{-2.35}$ (within the range of spectral index values deduced by Engelmann et al. 1990). Ionization energy loss, radioactive decay, spallation, and rates for attachment and stripping of single electrons on the GCR nuclei during propagation are incorporated in our model. For some of the species of interest in this study, the production and total fragmentation cross sections are not well-determined (see Appendix B for details). We use the energy dependence for partial fragmentation cross sections from Silberberg, Tsao, & Barghouty (1998, hereafter STB) and total fragmentation cross sections from Letaw, Silberberg, & Tsao (1983), renormalized for good agreement with the presently available set of cross section data, including those that were reported subsequent to STB (see Appendix B).

The ISM composition was assumed to be 90% H, 10% He by number (Peimbert 1975), consistent with solar photospheric measurements (Grevesse, Noels, & Sauval 1996), though the uncertainty in extending these abundances to the ISM may be significant (Strong & Moskalenko 1998). In order to understand uncertainties in this quantity on our

analysis, we have considered the effects of a 20% variation in the He/H ratio (He/H = 0.11 ± 0.02, from Peimbert 1975). Also of importance is the effect of ionized ISM gas on the determination of the mean path length. Soutoul, Ferrando, & Webber (1987) noted that the presence of ionized hydrogen in the ISM would increase the amount of GCR ionization energy loss during transport through an ISM of pure hydrogen by a factor of approximately 1.4, relative to ionization losses experienced in pure neutral hydrogen. This increase is based on observations by Harding & Harding (1985) of a 15% ionized fraction of ISM hydrogen. In our previous analyses (Yanasak et al. 1999, 2000, hereafter Y1999 and Y2000), we used a 24% ionized H fraction in the ISM, consistent with present observations of the scale heights and Galactic midplane densities of the ionized, neutral, and molecular H components (Nordgren, Cordes, & Terzian 1992; Diplas & Savage 1994; Dame et al. 1987). This value was also approximately consistent with the H ionized fraction of 28% used by DuVernois, Simpson, & Thayer (1996) in the *Ulysses* data analyses.

However, this ionization fraction is based on the assumption that GCR propagation occurs within a volume having a larger radius than the scale height of all of the ISM components. The characteristic distance through which GCRs diffuse, l, can be approximated using an equation similar to equation (1):

$$l \approx (Dt)^{1/2} . \tag{4}$$

In this equation, D is the GCR diffusion coefficient in the Galaxy, and t is the GCR lifetime against fragmentation in the ISM. Using the total fragmentation cross section from Westfall et al. (1979) to calculate the interaction length of ^{56}Fe in the ISM, the lifetime against fragmentation for Fe in an ISM of density $n_{\rm ISM} \sim 0.5$ atoms cm^{-3} is approximately 4.4 Myr. Using a typical diffusion coefficient of $D \sim 2 \times 10^{28}$ cm^2 s^{-1} (Ptuskin & Soutoul 1998a), the diffusion length is $\sim$530 pc, which is somewhat smaller than the scale height of the H^+ gas distribution. If one considers a fraction of this Fe to undergo escape ($\tau_{\rm esc} \sim 15$ Myr), the propagation lifetime $\tau_{\rm prop}$ will be smaller by $\sim$23%, and l will decrease to $\sim$400 pc. Integrating the density distributions for each gas component within a sphere of radius 400 pc, we find that the ionized fraction is consistent with a lower value of $H^+/H_{\rm tot} \sim 10\% \pm 4\%$. The error estimate assigned to the value of $H^+/H_{\rm tot}$ reflects the uncertainty in the molecular H density, the difference between the results from Nordgren et al. (1992) and Taylor & Cordes (1993) for the H^+ density, and the uncertainty in the size of the GCR propagation volume. One expects this estimate of the ionized fraction to be lower than the previous estimate because the smaller integration volume excludes a larger proportion of the ionized fraction of the ISM, which is most significant far from the Galactic disk.

The value of $\lambda_{\rm esc}$ was adjusted to account for secondary-to-primary elemental abundance ratios measured with CRIS. We examined the ratios B/C, P/S, (Sc+V)/Fe, and $(17 \le Z \le 25)$/Fe. *HEAO 3* data (Engelmann et al. 1990) were used as a consistency check of $\lambda_{\rm esc}$ at higher energies. Fitting the energy dependence of the secondary-to-primary ratios is critical for determining the ISM density and confinement time over the energy range of the data. As suggested by the work of Soutoul & Ptuskin (1999), we assume the following form of the escape mean free path:

$$\lambda_{\rm esc} = \frac{26.7\beta \text{ g cm}^{-2}}{(\beta R/1.0 \text{ GV})^{0.58} + (\beta R/1.4 \text{ GV})^{-1.4}} . \tag{5}$$

In this expression, R is the particle rigidity, and $\beta = v/c$, where v is the cosmic-ray velocity. This form for $\lambda_{\rm esc}$ has a stronger dependence on energy at lower energies than commonly used forms that assume $\lambda_{\rm esc} \propto \beta$, based on the concept of the diffusion of GCRs back into the Galactic disk competing with the outward convection of a dynamical Galactic halo (Jones 1979). Previous low-energy experiments have found that $\lambda_{\rm esc} \propto \beta^{3.5-4.5}$ is required to fit the observed energy dependences of secondary-to-primary ratios (e.g., Krombel & Wiedenbeck 1988; Garcia-Munoz et al. 1987). An energy dependence of $\lambda_{\rm esc}$ that is stronger than $\propto\beta$ provides a better fit for CRIS GCR secondary-to-primary ratios as well (Davis et al. 2000). Although we have adopted the form for $\lambda_{\rm esc}$ given in equation (5) on empirical grounds, its strong dependence on β at low energies is consistent with a model of Tan et al. (1987), which suggests that GCR diffusion at energies below 1 GeV nucleon^{-1} could be suppressed more effectively than at higher energies because of self-trapping by hydrodynamic waves generated by cosmic-ray streaming. Recent theoretical work suggests that a strong energy dependence of $\lambda_{\rm esc}$ could also result from a dependence of the velocity of a Galactic wind on the height above the Galactic disk (Soutoul & Ptuskin 1999). Alternatively, it has been suggested that the strong energy dependence observed in the low-energy B/C ratio could also be attributable to the effects of reacceleration (Strong & Moskalenko 1998). For the interstellar energy characteristic of the ^{10}Be measured by CRIS, $E \simeq 250$ MeV nucleon^{-1}, the mean path length traversed by the GCRs before escape is $\sim$6.7 g cm^{-2}.

Comparisons of the CRIS secondary-to-primary ratios with predictions from our LBM calculations using the expression for $\lambda_{\rm esc}$ given in equation (5) are shown in Figure 6. The CRIS data for B/C, P/S, and (Sc+V)/Fe are all reasonably well fitted with the same overall normalization of $\lambda_{\rm esc}$. In the case of P/S, (Sc+V)/Fe, and $(17 \le Z \le 25)$/Fe, a lack of fragmentation cross section data over a large range in energy adds uncertainty to the energy dependence of fragmentation in this model (see Appendix B), which may be the origin of the discrepancy between data and the model predictions for the $(17 \le Z \le 25)$/Fe ratio. The available cross section data are at energies similar to those sampled by CRIS in the ISM and probably account for the agreement at the lower CRIS energies. A single normalization for $\lambda_{\rm esc}$ was also found in some previous analyses (e.g., Engelmann et al. 1990), but others attempting to use a single exponential PLD ultimately required different normalizations for B/C and (Sc+V)/Fe ratios (e.g., Garcia-Munoz et al. 1987). We also note that DuVernois et al. (1996) find a suitable normalization for all secondary-to-primary ratios, but the experimental value of the *Ulysses* (Sc+V)/Fe ratio is below the CRIS measurement at a similar energy by $\sim$20%.

When a discrepancy between model fits for the lower Z secondary-to-primary ratios and the sub-Fe/Fe ratio was noted previously, weighted-slab PLDs with an energy-dependent truncation at shorter path lengths were suggested to resolve this discrepancy (e.g., Garcia-Munoz et al. 1987; Webber 1993). This could result from a concentration

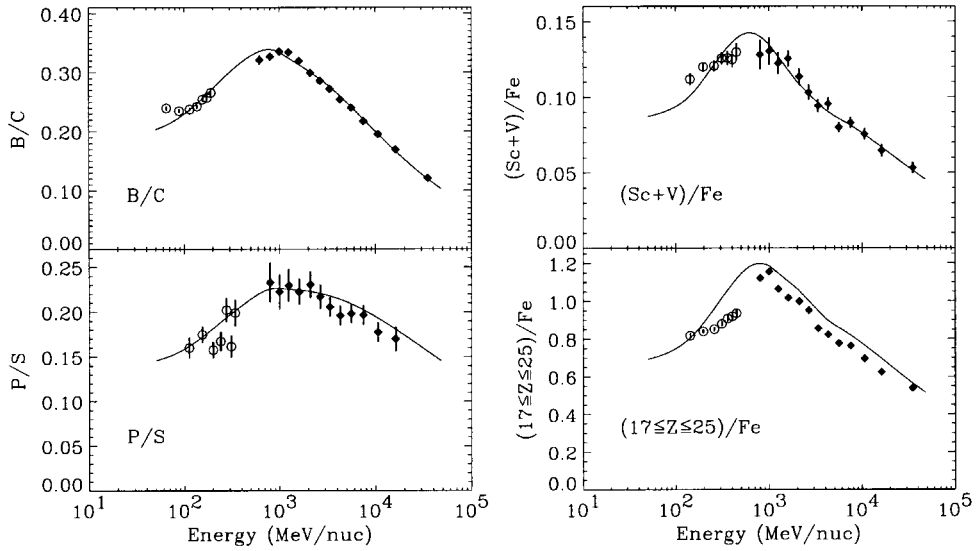

FIG. 6.—GCR secondary-to-primary ratios. The open circles are CRIS data, and the filled diamonds are data from *HEAO 3* (Engelmann et al. 1990). Also shown are theoretical curves from the propagation model described in this study.

of matter around discrete GCR sources in the Galaxy. Unlike our current study, our previous analyses (Y1999, Y2000) indicated a different normalization for the (Sc+V)/Fe ratio and the lower Z secondary-to-primary ratios measured by CRIS. However, the difference in normalization from that reported by Yanasak et al. (Y2000) is attributable entirely to the assumption of a lower ionization fraction in the ISM, based on a more detailed examination of the characteristic propagation volume. The increased energy loss in the ISM resulting from a larger assumed H^+ fraction, in conjunction with energy dependent fragmentation cross sections, decreases the amount of secondary production in the Fe group relative to lower Z secondaries. A similar effect was noted by Webber (1993), although his conclusions about the need for truncation were different, possibly because of the use of older fragmentation cross sections. Without stronger observational constraints on the H^+/H_{tot} ratio in the propagation volume, it appears difficult to separate the effects of PLD truncation and ionized fraction on the secondary-to-primary ratios.

Solar modulation of the cosmic-ray spectra was simulated with numerical solutions of a spherically symmetric Fokker-Planck model as described by Fisk (1971). In our solar modulation calculation, it is assumed that the interplanetary diffusion coefficient is proportional to βR and is independent of location in the heliosphere. Using this proportionality, the normalization of the diffusion coefficient corresponds to a modulation parameter $\phi = 325$ MV for GCRs in propagating from outside the heliosphere to 1 AU, using the relationship between ϕ and the diffusion coefficient defined by Gleeson & Axford (1968). This value for ϕ was obtained by comparing spectra from our LBM calculation to data from CRIS and *HEAO 3* (Davis et al. 2000). The value of modulation used in this study is different from the higher value from our earliest analysis ($\phi = 555$ MV, from Y1999). The previous value was based on the study by Badhwar & O'Neill (1993), which used the Climax neutron monitor as an indication of the level of cosmic-ray modulation. Subsequent work by ourselves (Davis et al. 2000) and others (A. Lukasiak 2000, private communication) showed that somewhat lower values of ϕ are more consistent with the solar minimum data from CRIS. Rather than assuming a modulation parameter and determining λ_{esc} with this constraint, our current study proceeded by finding the values for λ_{esc} and ϕ simultaneously that agree well with the CRIS data. To within the statistical accuracy of the CRIS data, the uncertainty in the value of ϕ is constrained to $\sim \pm 50$ MV. However, the possibility exists of a larger systematic uncertainty related to the technique used to find a modulation level or to the assumed rigidity dependence of the interplanetary diffusion coefficient. Consequences of an uncertainty in solar modulation will be discussed in the next section.

4. DISCUSSION

As described in § 3 above, the abundances of the secondary clock isotopes are used within the leaky-box model to derive a mean ISM density, ρ_{ISM}. Given the mean path length for escape and a mean ISM density, one can calculate the Galactic confinement time of GCRs from equation (3). Cosmic rays diffuse through the Galaxy, and because each clock species has a different mean lifetime, the volumes of the ISM through which each species diffuses will be somewhat different. The ISM matter distribution within the Galactic disk can vary dramatically over distance scales characteristic to GCR propagation (e.g., Frisch 1998), so ISM densities derived from LBMs need not be consistent among the various clock species. For example, using equation (1) for the diffusion distance and a typical diffusion coefficient $D \sim 10^{28}$ cm^2 s^{-1} (Ptuskin & Soutoul 1998a), ^{10}Be will sample a region within ~ 300 pc of the solar system, while ^{36}Cl will sample a region smaller by a factor $\sim [\tau(^{36}\mathrm{Cl})/\tau(^{10}\mathrm{Be})]^{1/2} \simeq 0.4$. Considering that the nominal scale height of the Galactic disk may be ~ 120 pc (Diplas & Savage 1994), the average ISM density determined from the abundance of ^{36}Cl may reflect the disk density more than the average density determined using ^{10}Be.

The left-hand column of Figure 7 compares predictions of the steady-state LBM discussed in § 3 for various assumed values of the ISM hydrogen number density, n_H, to CRIS abundances for the secondary radionuclides measured at Earth and those obtained previously from satellite observations aboard *Ulysses* (Connell 1998; Connell et al. 1998; DuVernois 1997; Simpson & Connell 1998), *ISEE 3*

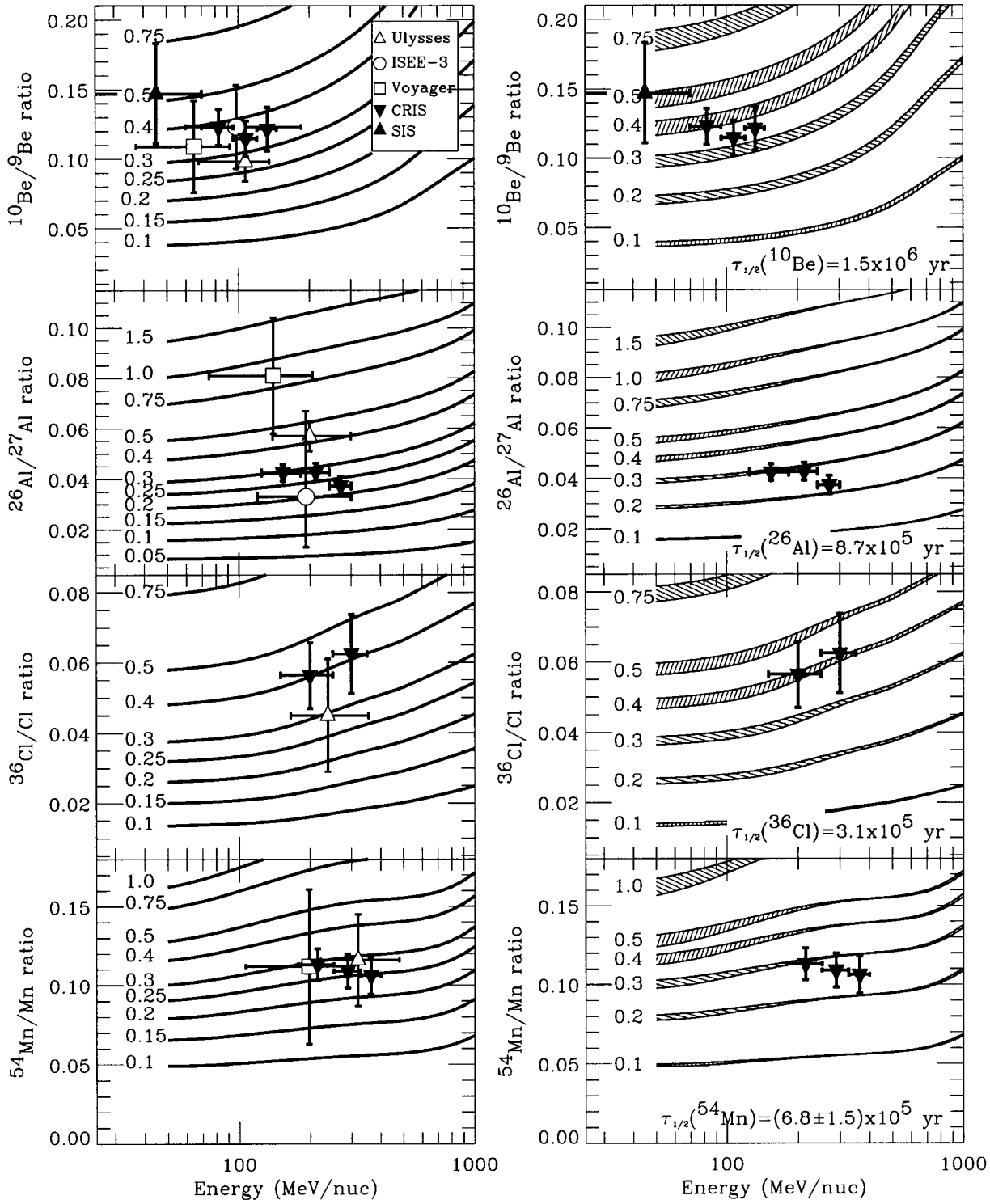

FIG. 7.—Secondary radionuclide abundance ratios from CRIS and previous satellite experiments as a function of energy. Curves in the first column of plots show model predictions for various assumed densities of ISM hydrogen in H atoms cm^{-3}. Ratios for the previous experiments have been adjusted to the level of solar modulation for CRIS as in Fig. 5. Hatched regions in the second column of plots show the variation in model predictions for constant ISM density assuming an uncertainty in the level of solar modulation $\Delta\phi = \pm 50$ MV. The half-life for ^{54}Mn comes from Wuosmaa et al. (1997) and Zaerpoor et al. (1999): $T_{1/2} = 0.68$ Myr. References for the data are as follows: *Filled downward triangle*, *ACE*/CRIS (this work); *filled upward triangle*, *ACE*/SIS (this work); *circle*, Wiedenbeck & Greiner (1980); Wiedenbeck (1983); *square*, Lukasiak et al. (1994a, 1994b); *open triangle*, Connell (1998); Connell et al. (1998); Simpson & Connell (1998); DuVernois (1997).

(Wiedenbeck & Greiner 1980; Wiedenbeck 1983), and *Voyager* (Lukasiak et al. 1994a, 1997a, 1997b). Previous abundance measurements were made at different periods in the solar cycle, and these have been adjusted to the level of modulation appropriate to CRIS as in Figure 5. In the cases such as *ISEE 3* where modulation is treated using a "force-field" model (Gleeson & Axford 1968), the force-field parameter, Φ, indicating the amount of modulation in energy units is converted to an analogous modulation parameter in rigidity ϕ using the following relation:

$\phi \approx (A/Z)\Phi$, where (A/Z) is assumed to be 2 (Gleeson & Axford 1968). To within statistical uncertainties, the density values derived from this model using the CRIS data are comparable to those obtained from previous calculations (Connell 1998). From Figure 7, the hydrogen number densities, n_H, obtained from the CRIS measurements of the various clock isotopes range from 0.27 to 0.43 H atoms cm^{-3}, with the highest densities indicated by the ^{36}Cl data. With our assumed ISM composition of 90% H, 10% He by number, this range corresponds to an ISM number density $(H + He)n_{ISM} = 0.30–0.48$ atoms cm^{-3}. As has been noted before (e.g., Garcia-Munoz et al. 1975), average ISM density values indicated by all of the secondary clock abundances in this study are less than the typically adopted disk density $n_{ISM} \sim 1$ atom cm^{-3}. In spite of its shorter half-life, the abundance of ^{36}Cl does not show any indication of an average ISM density that is significantly larger in its smaller propagation volume than those implied by the other radioactive secondary abundances. As discussed later in this section, the mean ISM hydrogen density and its weighted standard deviation considering both systematic and statistical uncertainties is $n_H = 0.34 \pm 0.04$ H atoms cm^{-3}. Using an ISM composition of 90% H, 10% He, this value corresponds to an ISM number density $n_{ISM} = 0.38 \pm 0.04$ atoms cm^{-3}. Considering only statistical uncertainties for each species, the mean hydrogen density is within 2 standard deviations of each individual density value.

Because of the high statistical significance of the CRIS data, the effect of systematic uncertainties in density predictions arising from uncertainties in model parameters such as the level of solar modulation and cross sections must be considered (see Appendix A). Hatched regions in the plots in the right-hand column in Figure 7 show the effect on the predictions for fixed ISM density when the level of solar modulation is varied by $\Delta\phi = 50$ MV. Differences in the modulation lead to greater change in the predictions for the $^{10}Be/^{9}Be$ ratio than for the other species because of the assumed rigidity dependence in the modulation diffusion coefficient and the larger A/Z difference between these isotopic species. A change in the solar modulation level $\Delta\phi = 50$ MV, equal to the amount of uncertainty mentioned in the previous section and shown in Figure 7, corresponds to a variation in the assumed ISM density of $\sim \pm 5\%$ from the ^{10}Be data. The other species show a somewhat smaller dependence on solar modulation uncertainties. Although uncertainties from statistics dominate, the contribution from modulation should not be neglected, being larger than 15% of the statistical uncertainty for the combined CRIS data and as large as 60% of the statistical uncertainty for ^{10}Be.

The deduced n_H from ^{54}Mn is in greatest statistical disparity with the mean density indicated by all species. However, interpretation of the abundance of ^{54}Mn is less certain because of its poorly known cosmic-ray half-life (see Table 1). In the laboratory, ^{54}Mn decays primarily via electron capture, with a 312 day half-life. However, in the cosmic rays, the fully stripped ^{54}Mn nuclei decay only by β^+- and β^--modes, with the β^+-decay half-life estimated to be ~ 500 times longer than the β^--decay half-life (Zaerpoor et al. 1997). In addition, the cross section for attachment of an electron to a bare ^{54}Mn nucleus is not negligible and is energy dependent, and this can complicate the interpretation of the ^{54}Mn abundance measurement (e.g., Wiedenbeck et al. 2000). Measurement of the β^--decay half-life in the laboratory has proceeded through the difficult direct detection of the decay (e.g., Kibedi et al. 1997), which has yielded only a lower limit on the lifetime and through indirect methods by observation of β^+-decay and inference of $T_{1/2}(\beta^-)$ from theoretical considerations (e.g., Zaerpoor et al. 1997; Wuosmaa et al. 1998). From the work of Zaerpoor et al. (1997, 1999) and Wuosmaa et al. (1998), the combined measurements of the β^+-decay imply a value for the β^--decay of $T_{1/2}(^{54}Mn) = (6.8 \pm 1.5) \times 10^5$ yr in the GCRs, which includes systematic and statistical uncertainties. From our model, a half-life uncertainty of $\pm 1.5 \times 10^5$ yr corresponds to a hydrogen ISM density uncertainty of $(-0.053, +0.079)$ H atoms cm^{-3}.

Progress is being made toward an accurate theoretical prediction of the ^{54}Mn β^--decay half-life. Recent theoretical calculations of the ^{54}Mn β^--decay half-life by Martinez-Pinedo & Vogel (1998) using a shell model calculation of β-decay rates indicate a value of $T_{1/2}(^{54}Mn) = (4.94 \pm 0.06) \times 10^5$ yr, smaller than what has been inferred from previous measurements of the ^{54}Mn β^+-decay half-life (Zaerpoor et al. 1999; Wuosmaa et al. 1998). The estimated uncertainty results from a particular theoretical consideration and does not necessarily reflect all theoretical uncertainties. Some disagreement exists in their predictions for other precisely measured β-decay half-lives as well, for reactions such as $^{26}Al(\beta^+)^{26}Mg$. G. Martinez-Pinedo & P. Vogel (1999, private communication) suggest that these differences result from a quenching factor affecting the absolute value of the nuclear form factor, which is removed by taking the ratio of β^--decay and β^+-decay half-lives. Multiplying the ratio of their predicted β^--decay and β^+-decay half-lives for ^{54}Mn with the experimental value of the β^+-decay half-life from Wuosmaa et al. (1998) and Zaerpoor et al. (1999) yields $T_{1/2}(^{54}Mn) = (6.0 \pm 1.2) \times 10^5$ yr for the β^--decay branch, in good agreement with calculations from earlier studies of the half-life for the β^--decay branch using β^+-decay half-life measurements. More work in this area is needed to resolve this discrepancy, including a direct measurement of the β^--decay of ^{54}Mn. At present, ^{54}Mn is useful as a consistency check between the propagation history of Fe-group elements and lighter species, while further interpretation of the ^{54}Mn abundance awaits a determination of the ^{54}Mn half-life with improved precision.

The densities indicated by the CRIS data may indicate a substantial amount of propagation in a local ISM cavity (Ptuskin & Soutoul 1998a). The recent survey by Diplas & Savage (1994) of n_H within the Galactic disk around the solar system finds an average neutral atomic hydrogen density component of 0.32 H atoms cm^{-3} in a cylindrical volume 2 kpc in radius and extending 240 pc above and below the Galactic disk. Previous surveys have found neutral hydrogen densities in a similar volume to be as much as $\sim 50\%$ larger (Diplas & Savage 1994). Combining this amount with the observed contribution of 0.1 H_2 molecules cm^{-3} from the local molecular hydrogen cloud density at the Galactic midplane (Dame et al. 1987) and 0.02 H^+ ions cm^{-3} from the ionized hydrogen density at the Galactic midplane (Taylor & Cordes 1993), the total hydrogen density n_H is approximately 0.54 H atoms cm^{-3} in the neighborhood of the disk around the solar system. Furthermore, the actual density within 240 pc of the solar system is less than this value by $\sim 11\%$ ($n_H \sim 0.47$ H atoms cm^{-3}), because the molecular cloud distribution about the Galactic disk is modeled as a Gaussian with an rms dispersion of 74

pc. This density is somewhat less than the typically assumed total density of 1 atom cm^{-3} ($n_H \sim 0.9$ H atoms cm^{-3}) given for the Galactic disk, which has been used to suggest significant propagation in a lower density halo (e.g., Simpson & Garcia-Munoz 1988). Although this explanation is not excluded, the Galactic disk hydrogen density result of $n_H \sim 0.47$ H atoms cm^{-3} is in less disparity with values derived from the CRIS data ($n_H = 0.34 \pm 0.04$ H atoms cm^{-3}) than are previous assumptions of $n_H \sim 0.9$ H atoms cm^{-3}, and significant halo propagation of the GCRs may not be required to explain the cosmic-ray clock observations.

The predicted energy dependence for all clock species is consistent with the data to within the statistical limitations of the observations, although the abundances of ^{26}Al from CRIS are also consistent with no energy dependence. Preliminary results from the cosmic-ray diffusion model of Strong & Moskalenko (1999) predict flatter energy dependences of the clock abundance ratios less than 1 GeV nucleon^{-1} than those given in our model (Fig. 7), somewhat more consistent with ^{26}Al but with similar consistency for the other species. Uncertainty in the energy dependence arising from uncertainties in the isotopic fragmentation cross section for production may also account for an additional 10% difference at most in the derived ISM density at lower energies (see Appendix B). Higher energy ^{10}Be data (Geier 2000) should provide a stronger test of the energy dependence of the Galactic confinement of GCRs, both because they will allow a wider range of time dilations to be sampled and because the higher energy abundances will be less affected by solar modulation.

Using the derived value of ρ_{ISM} for each species, the confinement times calculated from the CRIS clock abundances are presented along with previous experimental results in Table 4 and in Figure 8. The error bars shown for the CRIS data correspond to statistical and systematic uncertainties whose values are presented in Tables 4 (statistical) and 5 (systematic). Taken together with the additional systematic uncertainties presented in Table 5, the CRIS data imply a confinement time of $\tau_{esc} = 15.0$ Myr. Considering only the large systematic uncertainty in the half-life of ^{54}Mn (Wuosmaa et al. 1998; Zaerpoor et al. 1999) in addition to the statistical uncertainties, the confinement times for all species are consistent with this mean value to within 2 standard deviations.

The confinement times obtained from our model calculations are comparable to recent *Ulysses* results with the exception of ^{10}Be. Although the measured abundances of ^{10}Be from CRIS and *Ulysses* shown in Figure 7 and the reported values of n_{ISM} derived from these abundances agree, the derived confinement times do not. Part of this difference may result from the difference in the average

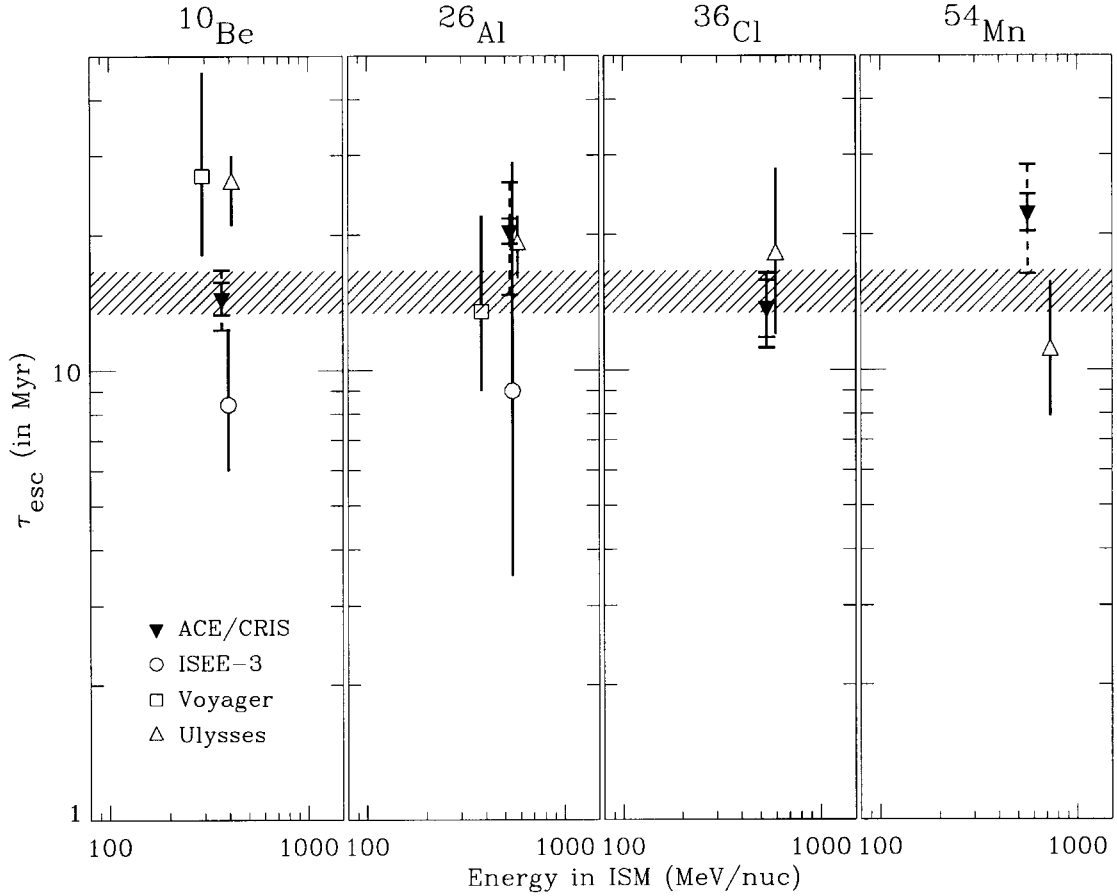

FIG. 8.—Confinement times obtained by CRIS and previous experiments. Data shown are from the references listed in the caption of Fig. 7. Uncertainties shown with solid error bars are 1 standard deviation statistical. The average value of the confinement time, $\tau_{esc} = 15.0 \pm 1.6$ Myr, indicated by the CRIS data for these four clock isotopes is shown as a hatched band. The dashed lines running through the CRIS data represent the uncertainty introduced from the combined systematic uncertainties shown in Table 5. The data point plotted for the *Ulysses* ^{54}Mn confinement time is based on the recalculation by Connell et al. (1998) using the ^{54}Mn decay half-life of $T_{1/2}(^{54}\text{Mn}) = 0.63$ Myr from Wuosmaa et al. (1998). Using the half-life of $T_{1/2}(^{54}\text{Mn}) = 0.68$ Myr assumed in this study raises the confinement time from *Ulysses* by ~ 1.5 Myr.

TABLE 4

MEAN CONFINEMENT TIMES AND SURVIVING FRACTIONS OF THE GALACTIC COSMIC-RAY CLOCK NUCLEI

Clock	$T_{1/2}$[a] (Myr)	Experiment	n_H[b] (H atoms cm^3)	τ_{esc}[b] (Myr)	f[b]	Reference
^{10}Be	1.5	*ACE*/CRIS	0.358 ± 0.032	14.5 ± 1.3	0.252 ± 0.018	This work
		Ulysses[c]	0.18 ± 0.03	$26.0^{+4.0}_{-5.0}$	...	1
		Voyager	$0.275^{+0.137}_{-0.113}$	$27.1^{+18.9}_{-9.0}$	...	2
		Voyager	$0.295^{+0.117}_{-0.099}$	...	0.259 ± 0.072	3
		ISEE 3	$0.30^{+0.12}_{-0.10}$	$8.4^{+4.0}_{-2.4}$	...	4
^{14}C	5.7×10^{-3}	*ACE*/CRIS	...	...	$<2.3 \times 10^{-2}$	This work
^{26}Al	0.87	*ACE*/CRIS	0.276 ± 0.018	20.4 ± 1.3	0.248 ± 0.012	This work
		Ulysses[c]	$0.24^{+0.05}_{-0.04}$	$19.0^{+3.0}_{-3.0}$	...	5
		Voyager	$0.52^{+0.26}_{-0.20}$	$13.5^{+8.5}_{-4.5}$	0.32 ± 0.09	6
		ISEE 3[d]	$0.25^{+0.65}_{-0.17}$	$9.0^{+20.0}_{-6.5}$	...	7
^{36}Cl	0.31	*ACE*/CRIS	0.425 ± 0.067	13.8 ± 2.2	0.155 ± 0.021	This work
		Ulysses[c]	$0.26^{+0.11}_{-0.09}$	$18.0^{+10.0}_{-6.0}$	...	8
^{54}Mn	0.68 ± 0.15	*ACE*/CRIS	0.267 ± 0.027	22.4 ± 2.3	0.284 ± 0.019	This work
		Voyager[e]	...	...	0.34 ± 0.15	9
		Ulysses[c,e]	$0.37^{+0.22}_{-0.14}$	$14.0^{+6.0}_{-4.0}$	...	10

[a] GCR half-lives shown include $\beta^{\pm}$-decay branches only.
[b] Quoted uncertainties are statistical.
[c] The term n_H recalculated from n_{ISM}, assuming 6.3% He, 93.7% H.
[d] The term n_H recalculated from n_{ISM}, assuming 10% He, 90% H.
[e] Assumes $T_{1/2} = 1$ Myr.

REFERENCES.—(1) Connell 1998. (2) Lukasiak et al. 1994a. (3) Lukasiak et al. 1997a. (4) Wiedenbeck & Greiner 1980. (5) Simpson & Connell 1998. (6) Lukasiak et al. 1994b. (7) Wiedenbeck 1983. (8) Connell et al. 1998. (9) Lukasiak et al. 1997b. (10) DuVernois 1997.

values of λ_{esc} used for converting derived values of ρ_{ISM} to corresponding values of τ_{esc}. We find $\lambda_{esc} \simeq 6.7$ g cm^{-2} for ^{10}Be obtained from CRIS at an ISM energy of 250 MeV nucleon^{-1} (see Table 2), and we estimate the path length for the *Ulysses* measurement at this energy to be $\lambda_{esc} \simeq 4.7$ g cm^{-2} from the formulation of the path length presented by DuVernois et al. (1996). Because the B/C ratio used to determine λ_{esc} in both studies is similar, this may be suggestive of differences in the total and partial fragmentation cross sections for the production of light secondaries used

TABLE 5

SOURCES OF UNCERTAINTY[a] IN COSMIC-RAY ISOTOPE SPECTROMETER DATA AND TRANSPORT MODEL

		MEASUREMENT		MODELING				
SPECIES	QUANTITY	Statistical	Background[b]	Solar Modulation[c,d]	Cross Section[e]	He/H[f,d]	H^+/H_{tot}[g,d]	Half-Life[h]
				H ISM Density, n_H (H atoms cm^{-3})				
^{10}Be	0.358	0.032	<0.001	0.018	0.042	0.008	...	...
^{26}Al	0.276	0.018	$^{+0.045}_{-0.061}$	0.003	0.062	0.006	...	...
^{36}Cl	0.425	0.067	$^{+0.011}_{-0.017}$	0.010	0.029	0.010	...	...
^{54}Mn	0.267	0.027	$^{+0.008}_{-0.012}$	0.002	0.005	0.006	...	$^{+0.078}_{-0.052}$
				Confinement Time, τ_{esc} (Myr)				
^{10}Be	14.5	1.3	<0.1	0.8	1.2	0.6	0.3	...
^{26}Al	20.4	1.3	$^{+5.8}_{-2.9}$	0.2	3.2	0.9	0.4	...
^{36}Cl	13.8	2.2	$^{+0.6}_{-0.3}$	0.3	0.5	0.6	0.3	...
^{54}Mn	22.4	2.3	$^{+1.1}_{-0.7}$	0.2	0.2	1.0	0.5	$^{+5.4}_{-5.1}$
				Surviving Fraction, f				
^{10}Be	0.252	0.018	<0.001	0.010	0.026	0.005	0.002	...
^{26}Al	0.248	0.012	$^{+0.030}_{-0.041}$	0.002	0.042	<0.001	0.002	...
^{36}Cl	0.155	0.021	$^{+0.003}_{-0.005}$	0.003	0.006	0.004	0.001	...
^{54}Mn	0.284	0.019	$^{+0.006}_{-0.008}$	0.001	0.003	0.004	0.003	<0.001

[a] Values given are nominally 1 standard deviation.
[b] Background from spillover of non-Gaussian tails from adjacent peaks in the mass histogram is calculated as a percentage of the area of the Gaussian fit to the adjacent peak (see § 2). The background subtraction and uncertainty is $0.7^{+0.7}_{-0.5}$ % of the adjacent peak area.
[c] The term $\phi = 325 \pm 50$ MV.
[d] Uncertainties are correlated between species.
[e] Calculation of uncertainties is described in Appendix B.
[f] ISM composition: He/H = 0.11 ± 0.02.
[g] ISM composition: $H^+/H_{tot} = 0.10 \pm 0.04$.
[h] The term $T_{1/2}(^{54}\text{Mn}) = 0.68 \pm 0.15$ Myr.

by the two groups (see Appendix B). However, this discrepancy cannot be attributed to differences between the weighted-slab model used in the *Ulysses* study and our steady-state model since weighted-slab models require larger values of the mean path length than steady-state models to account for secondary-to-primary ratios (Ptuskin et al. 1996; see also § 3). Interstellar compositional differences between these two models may also play a role; however, the greatest difference between the studies is the ionization fraction, which has greater influence on predictions of the sub-Fe/Fe secondary-to-primary ratio than of the B/C ratio.

As mentioned in § 3, the input parameters to the LBM in this study are somewhat different from those used in our previous analyses (Y1999, Y2000), and the effect of these differences on our derived values for $n_{\rm ISM}$ and $\tau_{\rm esc}$ deserves mention. The Y1999 study was a preliminary attempt to model GCR data from CRIS, relying more heavily on model parameters used in previous studies, which had not undergone a thorough reexamination. Upon further scrutiny of the model used in the Y1999 study, the solar modulation level (see § 3) and both partial and total fragmentation cross sections used in Y1999 required adjustment to match the current literature. The total fragmentation cross sections used in Y1999 for the Fe-group were found to be in slight disagreement with those shown in plots from STB and measurement data, and these were adjusted for Y2000 and this work. Furthermore, a comparison of partial cross sections for production of the GCR clocks used in the Y1999[2] study with more recent cross section data (see Appendix B) showed differences for some of the reactions, and these input cross sections were adjusted for agreement. In addition to these changes, investigation of the ionization fraction used in both Y1999 and Y2000 also revealed a value that was too high, as described in § 3, requiring different normalizations for $\lambda_{\rm esc}$ to account for the lower Z and the Fe-group secondary-to-primary ratios.

The effect of these adjustments is to require a different mean path length, changing the values of the confinement time and, in some cases, the average ISM densities from those we derive in this study. Adjustment of the partial fragmentation cross sections does not affect the mean path length but changes the required average ISM densities and the confinement time through equation (3). The parameter differences described above required our previous value of $\lambda_{\rm esc}$ in Y1999 to be $\sim$15% less than the value in this study in order to agree with all secondary-to-primary ratios except for sub-Fe/Fe. In the case of the latter ratio, the combined errors in choosing an ionization fraction and total fragmentation cross sections in Y1999 effectively negated, resulting in a similar Fe-group mean path length for Y1999 and this study. Comparing the Y2000 study with the present work, the value of $\lambda_{\rm esc}$ is appreciably different only for the Fe-group species, so the confinement time for ^{54}Mn is the only quantity significantly changed in our current analysis.

Within the framework of the leaky-box model, the surviving fraction probes the average ISM density during the species lifetime once the abundances of stable secondaries constrain the escape mean free path. In Figure 9 and Table 4 we present the surviving fractions given by our LBM for each clock, including our upper limit on the fraction of ^{14}C. The curves shown in Figure 9 were calculated using equation (A8) in Appendix A, which results from a steady-state LBM that neglects energy loss. As Figure 9 demonstrates, the predictions of f from equation (A8) using model parameters appropriate for ^{10}Be do not agree exactly with the surviving fractions calculated with our LBM (which includes energy loss) using measurements for each species. The fraction for the shorter-lived isotope ^{36}Cl is in greater disagreement from the curves than ^{10}Be or ^{26}Al and may indicate a slightly higher ISM density than the value derived from the ^{10}Be measurements. Considering the relatively small range of half-lives between ^{10}Be and ^{36}Cl [$T_{1/2}(^{10}\mathrm{Be})/T_{1/2}(^{36}\mathrm{Cl}) \simeq 5$] and the fact that the diffusion distances to which these correspond scale as $(\tau_{\rm decay})^{1/2}$ (see eq. [1]), these species may not be particularly sensitive probes of local inhomogeneities in the ISM matter distribution. However, longer distance scales can be probed by measuring radioactive nuclide abundances at energies where time dilation extends the decay half-lives (e.g., Geier 2000). To probe smaller distance scales, the surviving fraction for ^{14}C should be more precisely determined to provide a more complete picture of local inhomogeneity over a broad range of characteristic distances. Presently, the upper limit on the ^{14}C abundance from CRIS does not provide a strong constraint on the interstellar density encountered by cosmic rays in the region close to the solar system.

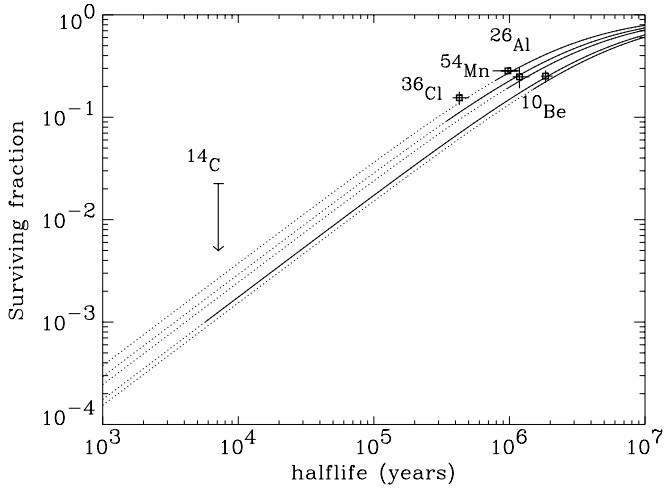

FIG. 9.—Surviving fractions, f, of the secondary radionuclides in the ISM as a function of half-life. The horizontal error bars correspond to the approximate range in half-lives from time dilation at ISM energies for each species. Vertical error bars indicate the amount of statistical and systematic error in the calculation of the surviving fractions (see Table 5). Also shown are curves based on a leaky-box model of propagation relating surviving fraction to half-lives of arbitrary duration, assuming differences in the fragmentation mean free path appropriate for secondary nuclei with masses equal to $A = 10$, 14, 26, 36, and 54. The curves are extended below the minimum GCR half-life for each species using dotted lines to show the trend given by eq. (A8). These curves increase in surviving fraction for a given value of half-life as mass increases. For this calculation, corrections for time dilation appropriate to ISM energies for each species are included. The curves are calculated using the confinement time and mean ISM density deduced from ^{10}Be. Energy loss during propagation is not considered in the calculation of the model curves.

[2] The cross sections for the Y1999 study were evaluated using version v1993 of software from the Space Physics Data System node at the Louisiana State University based on the work of Webber, Kish, & Schrier (1990b), available at http://spdsch.phys.lsu.edu/SPDSCH_Pages/Software_Pages/Software.html.

The values of f shown in Table 4 were calculated from the abundances of the secondary radionuclides using our LBM model, and one must be careful in comparing predictions of f calculated using an LBM to values of f derived from diffusion models. In diffusion models, the surviving fractional abundance of a radioactive secondary is indicative of the fraction of secondary production within a characteristic volume $\propto r^3$ around the solar system, which scales according to the diffusion distance during its lifetime, l, given by equation (1): $r \sim l$. Nuclei produced beyond this distance will generally decay before detection. This relationship allows one to estimate the diffusion coefficient D for a propagation model given a particular ISM matter distribution. Recent work (e.g., Ptuskin, Soutoul, & Streitmatter 1999; Simon & Molnar 1999) suggests that f calculated using LBM and diffusion models will be somewhat different at CRIS energies for ^{26}Al and ^{36}Cl if the input model parameters are chosen to account for the abundance of ^{10}Be. Ptuskin & Soutoul (1998b) have previously discussed the relationship between LBMs and models assuming isotropic diffusion for stable secondaries, showing that the ratio of Galactic halo scale height, H, and galactic disk half-thickness, h, must obey the inequality $\lambda_{i,\mathrm{spall}}/\lambda_{\mathrm{esc}} \gg h/H$ for both models to yield equivalent abundance predictions. In this expression, $\lambda_{i,\mathrm{spall}}$ is the fragmentation interaction length for GCR species i. This condition stipulates that the loss of GCR nuclei by fragmentation be negligible during a single crossing of the transport region (Ptuskin & Soutoul 1998b). In addition, a more stringent condition of $l^2 \gg h^2$ is required for similar predictions for secondary radioactive species (Ptuskin & Soutoul 1990). This inequality insures that the radioactive clock species have diffused through the Galactic disk over much larger distance scales than those characteristic of the ISM density variations, assumed to be smaller than h. Otherwise, clock abundances would be strongly influenced by local inhomogeneities, and τ_{esc} and n_{ISM} derived from surviving fractions in the LBM would not correspond to equivalent quantities in the diffusion model.

From equation (A8) in Appendix A, $J_{i,\mathrm{nodecay}}$ is the abundance of secondary clock particles that survive transport assuming no decay, which should be the same predicted quantity in LBM and diffusion models if the above condition for H/h holds. At CRIS energies, the ratio of $\lambda_{i,\mathrm{spall}}/\lambda_{\mathrm{esc}}$ for $Z = 6$–26 ranges approximately from 1.25 for C to 0.55 for Fe, so $H/h \gg (0.8$–$1.8)$ is the condition for stable secondary abundance predictions to agree between the models. Typical halo heights employed in diffusion models may range from 1–10 kpc, and astronomical measurements tend to agree with these values (Ptuskin & Soutoul 1998b). Taken together with a Galactic disk half-thickness $h \sim 100$ pc, the condition for H/h is satisfied. In the case of $J_{i,\mathrm{decay}}$, one requires $l^2 \gg h^2$ for similarity between LBM and diffusion model predictions for radioactive secondary abundances. Using $D = 1 \times 10^{28}$ cm^2 s^{-1}, the range in l varies from 310 pc for ^{10}Be to 140 pc for ^{36}Cl at CRIS energies, which implies that f may differ between LBM and diffusion models depending on whether the species is long-lived or not. If the diffusion coefficient is significantly larger, then this condition may be met by ^{26}Al and ^{36}Cl at CRIS energies as well as ^{10}Be.

The geometry of the ISM matter distribution for diffusion models is not well constrained by observation and, in general, the interpretation of clock abundances is specific to a particular choice of geometry. Ptuskin & Soutoul (1998a) calculated the relationship between f and D for the secondary radionuclides using models with a variety of geometries for the distribution of ISM material. Their predictions for the surviving fraction of ^{10}Be are plotted as curves in panel a of Figure 10 for an energy $E = 400$ MeV nucleon^{-1}, slightly higher than the range of ISM energies of the ^{10}Be data measured with CRIS and similar to the ISM energies for ^{26}Al and ^{36}Cl data (see Table 2). Curves I and II result from simple geometries, with the ISM gas distribution confined to an infinitely thin disk for curve I and a single layer distribution with an exponential profile along the dimension z perpendicular to the disk for curve II. Curve III assumes a gas distribution with three components having separate exponential profiles in z, corresponding to components of the gas at different temperatures. Curve IV is

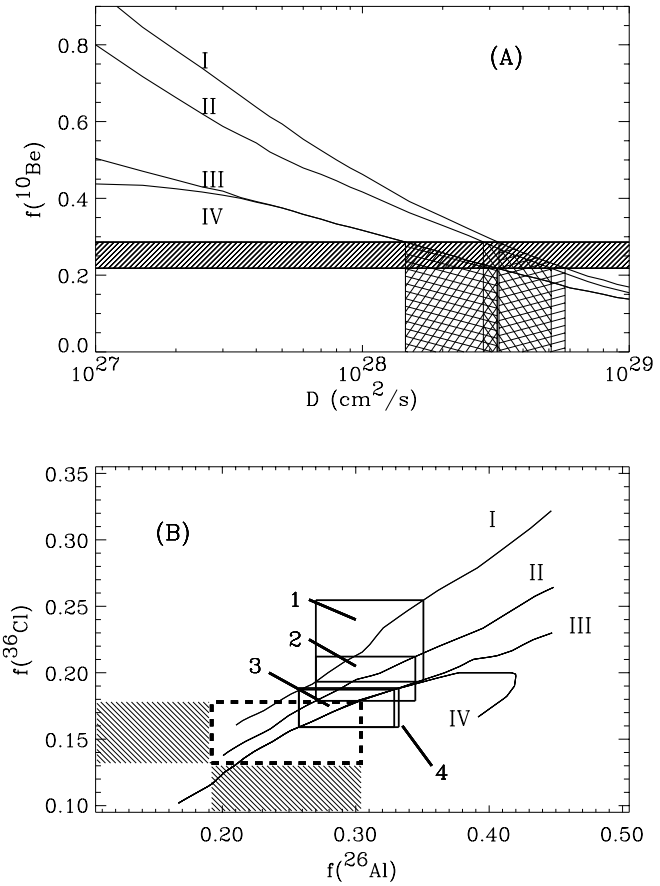

FIG. 10.—Surviving fractions, f, of ^{10}Be, ^{26}Al, and ^{36}Cl. Panel a shows the surviving fraction of ^{10}Be as a function of the local diffusion coefficient D. Curves are adapted from diffusion model calculations by Ptuskin & Soutoul (1998a). The horizontal hatched region shows the CRIS results from this study (Table 4). The vertical hatched regions correspond to values of D allowed by the ^{10}Be data for each model. Panel b shows model predictions for the relationship between the surviving fractions of ^{26}Al and ^{36}Cl for different values of D. The dashed box and the hatched regions represent f from ^{26}Al and ^{36}Cl abundances measured by CRIS (Table 4). The boxes with a solid border are allowed values of f for each species, given the constraint on D from each model using the ^{10}Be surviving fraction. Boxes appropriate to each model are labeled in Arabic numerals. Note that boxes for models III and IV (labeled "3" and "4") overlap significantly. Model descriptions: I, Galactic disk of infinitesimal thickness; II, single gas layer distributed exponentially along an axis perpendicular to the Galactic plane; III, three superposed gas layers with exponential distributions having differing scale heights; IV, same as III but with a 200 pc radius cylindrical cavity of full height 260 pc around the solar system.

identical to the distribution of curve III with the exception of a cylindrical cavity evacuated around the solar system of radius 200 pc and full height 260 pc based on the observations of Paresce (1984) and others. Values of f obtained from the CRIS data using the LBM calculations are shown as horizontal hatched regions extending across panel *a*, assuming 1 standard deviation uncertainties including both systematic and statistical errors. Also shown are the range of values of D over which the surviving fractions from CRIS overlap with the predictions from each model curve, plotted as vertical hatched regions. A comparison of the values of $f(^{10}\mathrm{Be})$ from CRIS to the model curves yields a local diffusion coefficient D ranging from $\sim 1.5 \times 10^{28}$ cm^2 s^{-1} to 5.5×10^{28} cm^2 s^{-1}, with a typical value of D within these models of $\sim 3.5 \times 10^{28}$ cm^2 s^{-1}.

Panel *b* of Figure 10 compares predictions from each model to the surviving fractions for ^{36}Cl, ^{26}Al, and ^{10}Be. Assuming a consistent value for D between species, each model described above predicts a relationship between $f(^{36}\mathrm{Cl})$ and $f(^{26}\mathrm{Al})$, shown as curves in panel *b*. The box bordered by a dashed line shows the surviving fraction deduced from CRIS measurements within 1 standard deviation for these two species, including statistical and systematic uncertainties. Using the range in values for D derived from the surviving fraction for ^{10}Be in panel *a*, one can predict the surviving fractions for the other two species, and these predictions for each model are shown as boxes with a solid border in panel *b*. The Arabic numerals denote the model from which the range of D was chosen using $f(^{10}\mathrm{Be})$. The overlap between boxes indicates consistency between models. From Figure 10, the models with three gas components (III and IV) appear to be favored, and the simple model I appears the least consistent with the surviving fraction data from CRIS. However, the boxes represent 1 standard deviation, so this result does not strongly constrain the model geometry. Introduction of a low-density cavity of radius 200 pc around the solar system does not affect D greatly for $D = 4 \times 10^{28}$ cm^2 s^{-1} since these isotopes diffuse significantly larger distances than the size of the cavity in their lifetimes. The difference between predictions of the fraction for the shorter lived species ^{14}C is potentially a stronger test. However, the present CRIS upper limit to the surviving fraction of ^{14}C does not significantly constrain the ISM matter distributions investigated by Ptuskin & Soutoul (1998a).

The values of n_{H}, τ_{esc}, and f from our LBM and associated uncertainties are presented in Table 5 (see also Appendix A). Statistical uncertainties, while much improved over previous measurements, continue to be significant. However, the uncertainty in partial fragmentation cross sections contributes a comparable amount of uncertainty, originating from the small number of available cross section measurements for some reactions. Cross section uncertainties for ^{36}Cl and ^{54}Mn, although smaller than statistical uncertainties, are estimated from the differences in the theoretical cross section formulae of STB and Webber, Kish, & Schrier (1990b, hereafter WKS). A more realistic estimate may be at least as large as the uncertainty contribution for species with a larger number of cross section measurements such as ^{26}Al, which results from inconsistencies in fragmentation data (see Appendix B).

Uncertainty in the ISM ionization fraction affects the determination of λ_{esc}. Uncertainty in the mean path length has a greater influence on the value of the confinement time for ^{54}Mn than on the other clock species because the path length for fragmentation is shorter for Fe-group species than for lighter GCR species. As discussed in § 3, the ionization fraction adopted for this study is $\mathrm{H}^+/\mathrm{H}_{\mathrm{tot}} = 10\% \pm 4\%$ (Taylor & Cordes 1993; Diplas & Savage 1994; Dame et al. 1987), and the confinement times and uncertainties in Table 5 assume this value of the ionization fraction and this uncertainty. However, if the uncertainty in the ionization fraction is significantly larger and its value is closer to ~20%–30% as indicated by some previous studies (e.g., DuVernois et al. 1996), the confinement time given by the ^{54}Mn abundance will increase by ~13 Myr, while the confinement times indicated by other species increase by ~1 Myr. As mentioned previously, the most significant uncertainty affecting the transport parameters derived from ^{54}Mn continues to be the value of its half-life.

The mean ISM hydrogen density, calculated by weighting the densities for all four species using the statistical and systematic uncertainties given in Table 5, is $n_{\mathrm{H}} = 0.34 \pm 0.04$ H atoms cm^{-3}. This calculation of the weighted standard deviation around the mean assumes that density uncertainties resulting from uncertainty in solar modulation and ISM composition are correlated between species. The standard deviation given by the distribution of the four measured density values around 0.34 atoms cm^{-3} is ± 0.08 atoms cm^{-3}. If the correlated uncertainties are excluded for simplicity, the reduced χ^2 value calculated comparing the four density values with the mean value is 0.77, indicating that the four individual density values are consistent with a single value of the ISM density.

Calculated in a similar manner, the mean confinement time and the weighted standard deviation from statistical and systematic uncertainties is $\tau_{\mathrm{esc}} = 15.0 \pm 1.6$ Myr. From the distribution of the individual confinement times around the mean, the standard deviation is 4.6 Myr, which is larger than the weighted standard deviation. However, some of this difference can be accounted for by the large uncertainty in the measurement of the Mn half-life. Excluding the ^{54}Mn measurement, the mean confinement time and weighted standard deviation is 14.6 ± 1.6 Myr, and the rms spread of confinement times around the mean is 3.4 Myr.

5. CONCLUSIONS

We have presented isotopic abundance measurements for the GCR secondary radionuclides ^{10}Be, ^{26}Al, ^{36}Cl, and ^{54}Mn and an upper limit for ^{14}C obtained using the CRIS instrument on *ACE*. We have developed a consistent interpretation of these abundances in the context of GCR propagation by using a steady-state, leaky-box model consistent with current observations of the composition of stable cosmic rays and with the composition and density of matter in the local ISM.

The observed abundances of all secondary radionuclides are adequately accounted for by a Galactic confinement time of $\tau_{\mathrm{esc}} = 15.0 \pm 1.6$ Myr, including statistical and systematic uncertainties. This corresponds to an average ISM hydrogen number density $n_{\mathrm{H}} = 0.34 \pm 0.04$ H atoms cm^{-3} for propagation through the mean path length of matter described in § 3. Subdividing the data into multiple energy bins indicates an energy dependence for these abundances that is consistent with the increase of the radioactive isotope abundances with increasing energy expected from leaky-box or diffusion models (e.g., Strong & Moskalenko

1999) or with no energy dependence over the range of measured energies. The abundance of ^{36}Cl requires a value for n_H during propagation that is consistent with average densities indicated by the longer lived species. Assuming isotropic diffusion, this may indicate that the size of the propagation volume for ^{36}Cl does not make the abundance of this species particularly sensitive to ISM mass density differences between the Galactic disk and the lower density halo.

Comparing the surviving fractional abundances to predictions from the diffusion models of Ptuskin & Soutoul (1998a) suggests a value for the cosmic-ray interstellar diffusion coefficient of $D = (3.5 \pm 2.0) \times 10^{28}$ cm^2 s^{-1}. The abundances of ^{26}Al and ^{36}Cl do not appear to favor their simplest model geometry of a thin gas disk when compared to the value of D derived using the surviving fraction of ^{10}Be. The upper limit on the abundance of ^{14}C presented in this work is not sufficiently stringent to provide significant new constraints on the distribution of matter sampled by cosmic rays in the immediate neighborhood of the solar system.

We gratefully acknowledge the individuals responsible for the development of the CRIS instrument (listed in Stone et al. 1998a). We appreciate the helpful discussion of Petr Vogel concerning theoretical calculations of the half-life of ^{54}Mn. We also thank the University of Chicago for providing Climax neutron monitor data (supported by National Science Foundation grant ATM 96-13963).

This research was supported by the National Aeronautics and Space Administration at the California Institute of Technology (under grant NAG5-6912), the Jet Propulsion Laboratory, the Goddard Space Flight Center, Washington University, and the McDonnell Center for the Space Sciences at Washington University.

APPENDIX A

RELATIONSHIP BETWEEN MODEL UNCERTAINTIES, CONFINEMENT TIME, AND INTERSTELLAR MEDIUM DENSITY

In addition to statistical uncertainties in measured abundances, uncertainties in the physical parameters required as input to a leaky-box model limit the ability to determine the confinement time, τ_{esc}, and the average ISM density, ρ_{ISM}. For a GCR nuclide of species i at a particular ISM energy per nucleon E, the steady-state equation (Meneguzzi et al. 1971) governing its number density, J_i, during transport in a leaky box assuming a simple exponential PLD is given by

$$0 = -\frac{J_i}{\lambda_{esc}} + \frac{\partial}{\partial E}(\omega_i J_i) - J_i\left\langle \frac{\sigma_i}{\mathcal{M}} \right\rangle - \frac{J_i}{\rho_{ISM}\beta c\gamma\tau_i} + Q_i\,, \tag{A1}$$

where the production term Q_i is given as

$$Q_i = \sum_j J_j\left(\left\langle \frac{\sigma_{j,i}}{\mathcal{M}} \right\rangle + \frac{1}{\rho_{ISM}\beta c\gamma\tau_{j,i}}\right) + q_i\,. \tag{A2}$$

Here, the sum over j includes all parent species j that can undergo decay or fragmentation into the daughter product i. The quantity in the fragmentation term is defined as

$$\left\langle \frac{\sigma}{\mathcal{M}} \right\rangle \equiv \frac{n_H\sigma^H + n_{He}\sigma^{He}}{\rho_{ISM}}\,. \tag{A3}$$

In these equations, $n_{ISM} = n_H + n_{He}$ is the ISM number density ($\rho_{ISM} \equiv \mathcal{M}_H n_H + \mathcal{M}_{He} n_{He}$, where $\mathcal{M}$ is the ISM atom mass), σ_i is the total fragmentation cross section for species i, $\sigma_{j,i}$ is the partial cross section for the fragmentation of j into i, τ_i is the mean lifetime of species i against decay, $\tau_{j,i}$ is the mean lifetime of species j before its decay to species i, $\omega_i \equiv (dE/dx)_i$ is the ionization energy loss of species i per unit path length x in the ISM, and q_i represents the primary production of species i by the GCR source. The superscripts for the cross sections in equation (A3) indicate the target nucleus for the fragmentation reaction in the ISM. The terms for loss or gain via radioactive decay apply only for specific species.

Solving equation (A1) for the steady-state GCR intensities yields

$$J_i(E) = \frac{Q_i}{1/\lambda_{esc}(E) + \langle\sigma_i/\mathcal{M}\rangle_{ISM}(E) + 1/\rho_{ISM}\beta c\gamma\tau_i - 1/\lambda_{i,\omega}(E)}\,, \tag{A4}$$

where we have expressed the energy-loss term for species i in terms of a characteristic path length for energy loss $\lambda_{i,\omega}$. This energy-loss path length is given by

$$\frac{1}{\lambda_{i,\omega}} = \frac{\partial\omega_i}{\partial E} + \psi\,\frac{\omega_i}{E}\,, \tag{A5}$$

where $\psi \equiv \partial \ln J_i/\partial \ln E$ is the GCR spectral index at a given energy. From equation (A4), a measurement of the abundance ratio of a stable secondary species s to a single primary parent p constrains the mean path length through the following relationship:

$$\frac{J_s}{J_p} = \frac{Q_s}{Q_p}\,\frac{1/\lambda_{esc} + \langle\sigma_p/\mathcal{M}\rangle + 1/\lambda_{p,\omega}}{1/\lambda_{esc} + \langle\sigma_s/\mathcal{M}\rangle + 1/\lambda_{s,\omega}}\,. \tag{A6}$$

After some rearranging of terms, we find

$$\lambda_{\rm esc}(E) = \frac{(J_s/J_p)/(Q_s/Q_p) - 1}{\langle \sigma_p/\mathscr{M} \rangle + 1/\lambda_{p,\omega} - (\langle \sigma_s/\mathscr{M} \rangle + 1/\lambda_{s,\omega})(J_s/J_p)/(Q_s/Q_p)} \,. \tag{A7}$$

The source term for secondary GCRs, Q_s, following from equation (A2) is a function of the GCR primary's equilibrium abundance, J_p, during transport and the cross section for the fragmentation of primary particles to the secondary species. So we find that our ability to derive $\tau_{\rm esc}$ and the average ISM density using information about $\lambda_{\rm esc}$ and equation (3) (see § 3) is limited by fragmentation cross sections, ISM compositional uncertainties, and uncertainties in the rate of GCR energy loss in the ISM. Varying the assumed fraction of ionized material in the ISM can lead to different energy loss rates during the transport lifetime of the GCRs, as noted by Soutoul et al. (1987).

Using the steady-state LBM solution in equation (A4) above, the sources of uncertainty in determining $\tau_{\rm esc}$ and $\rho_{\rm ISM}$ from the surviving fractional abundance of a secondary clock can be shown. Equation (2) in § 3 follows from the steady-state solution of the LBM transport equation. Using equations (3), (A3), and (A4) and neglecting energy loss, we can write the surviving fraction, f, as

$$f \equiv \frac{J_{i,\,\rm decay}}{J_{i,\,\rm no\ decay}} = \frac{1/\tau_{\rm esc} + (n_{\rm H}\,\sigma_i^{\rm H} + n_{\rm He}\,\sigma_i^{\rm He})\beta c}{1/\tau_{\rm esc} + (n_{\rm H}\,\sigma_i^{\rm H} + n_{\rm He}\,\sigma_i^{\rm He})\beta c + 1/\gamma\tau_{i,\,\rm decay}} \,. \tag{A8}$$

As this expression demonstrates, uncertainties in $\tau_{\rm esc}$ and the average ISM density originate from ill-determined fragmentation cross sections, uncertainties in the ISM composition $n_{\rm H}/n_{\rm He}$, and uncertainties in $\lambda_{\rm esc}$, which relates $\tau_{\rm esc}$ and $\rho_{\rm ISM}$. However, the comparison of $\tau_{\rm esc}$ and the average ISM density using multiple species will help to decrease the contribution to the uncertainty from cross sections, which are generally uncorrelated between species.

APPENDIX B

PARTIAL FRAGMENTATION CROSS SECTIONS

A source of uncertainty that can significantly affect the determination of $\rho_{\rm ISM}$ and $\tau_{\rm esc}$ is the small number of available measurements of some of the relevant isotopic fragmentation cross sections at cosmic-ray energies. Measurements exist for several reactions involving primary species such as ^{56}Fe(p,*)^{36}Cl that are important for understanding the production rate of the secondary radionuclides at interaction energies similar to those probed by the CRIS measurements (e.g., see Table 6 for references used in our propagation model). However, many reaction cross sections either have not been measured or have been studied only at one or two energies. The lack of measurements and the existence of systematic differences between cross section experiments limits the ability to predict the energy dependence of fragmentation over a wide range of energies. STB and WKS have used an extensive set of cross section measurements to derive formulae that predict the isotopic fragmentation cross sections for most of the reactions for production from primaries with $Z \leq 26$. However, these two formulations of the energy dependence frequently differ significantly where they are not well constrained by data. For our study, we use the energy dependences from STB. Although the STB energy dependences are based on a sizable subset of the references in Table 6 as well as on other data at lower and higher energies, their calculations do not always adequately account for the measurements in the energy range relevant for the CRIS analysis. To obtain better agreement, we normalized the STB curves to experimental cross section values reported in the references listed in Table 6, taking into account the statistical weight of the measurement.

Constraining the production is more problematic for ^{10}Be, in particular, than for the other species. Because the data in this study were accumulated during a period of solar minimum, the cosmic rays observed by CRIS have experienced relatively little solar modulation during transport into the heliosphere. Consequently, the ISM energy range for data in this study is lower than for observations made on *Ulysses* (Connell 1998) and *ISEE 3* (Wiedenbeck & Greiner 1980). For a modulation level appropriate to CRIS, the higher end of the ISM energy range for the other radioactive secondary clocks is near or overlaps with the reaction energy $E \simeq 600$ MeV nucleon^{-1}, at which many of the cross section measurements were made (see Table 2). However, the approximate ISM energy range for ^{10}Be is somewhat lower, $\sim$120–350 MeV nucleon^{-1}. Although measurements exist below this energy range for a number of the important parent nuclei, the expressions of STB and WKS do not agree with both the measurements above and below this range in some cases.

Figure 11 shows cross section measurements for the production of ^{9}Be and ^{10}Be as a function of energy for a few of the important parent nuclei for which measurements exist. In addition, measurements for the reactions ^{11}B(p,*)^{9}Be and ^{11}B(p,*)^{10}Be exist but show inconsistency, and these data are plotted in Figure 11 as an illustration of large measurement discrepancies for some reactions. The nuclei from the CNO group contribute $\sim$80% to the total observed GCR Be. Although nitrogen contributes significantly to the production of Be as well as carbon and oxygen, the data are too sparse and have uncertainties that are too large to show any marked disagreement with the theoretical curves of STB or WKS. The hatched band shows the ISM energy interval relevant to the CRIS Be data. The dotted curves represent the cross sections given by the WKS formulae, and the dashed curves are those predicted by STB, both normalized to the data as mentioned above. The software that calculates the cross sections using the STP and WKS formulae is based on a code distributed by the Louisiana State University on their Space Physics Data System World Wide Web site (see the footnote in § 4 for more detail). Although formulae from both of the groups predict similar behaviors, such as an asymptotic value at higher energies, neither group predicts an energy dependence in good agreement with the lower energy data for all important parent nuclei. Rather than

TABLE 6

REFERENCES FOR PARTIAL CROSS SECTION MEASUREMENTS AT COSMIC-RAY ENERGIES

Clock Isotope	Parent Primary Species[a]	Reference
^{10}Be.....	C, Al, Ca	1, 2
	N	1, 2, 3
	O	1, 2, 4
	Mg	1, 2, 3, 5, 6
	Si	1, 2, 3, 4, 5, 6
	Fe	1, 2, 5, 7
	^{11}B	8, 9, 10
	^{12}C	8, 9, 11, 12, 13, 14, 15, 16, 17
	^{13}C	14, 18
	^{14}N	9
	^{16}O	6, 13, 19, 20
^{14}C.....	^{16}O, ^{20}Ne	8, 9
	^{14}N, ^{15}N	8
	^{22}Ne	8, 22
	^{26}Mg	22
^{26}Al.....	O	4
	Si	1, 2, 4
	Ca	1
	Al, Fe	1, 2
	^{27}Al, ^{28}Si, ^{32}S	9, 21
	^{36}Ar	21, 23
	^{40}Ar	23
	^{29}Si, ^{30}P, ^{31}P, ^{33}S, ^{38}Ar	21
	^{40}Ca	24
^{36}Cl.....	Ca, Fe	1, 2, 25
	^{36}Ar	21, 23
	^{40}Ar	23
	^{40}Ca	24
	^{37}Cl, ^{38}Ar, ^{54}Fe, ^{55}Mn	21
^{54}Mn	Fe, Ni	1, 2
	^{56}Fe	8, 9

[a] Parent species with no listed mass number indicates that the experimental target was composed of a terrestrial mix of isotopes.

REFERENCES.—(1) Schiekel et al. 1996a. (2) Michel et al. 1995. (3) Raisbeck & Yiou 1974. (4) Sisterson et al. 1997. (5) Raisbeck & Yiou 1975. (6) Raisbeck & Yiou 1977. (7) Perron 1976. (8) Webber et al. 1998b. (9) Webber et al. 1990a. (10) Raisbeck & Yiou 1976. (11) Korejwo et al. 1999. (12) Webber & Kish 1985. (13) Lindstrom et al. 1975. (14) Yiou et al. 1973. (15) Fontes et al. 1971. (16) Lestringuez et al. 1971. (17) Cumming 1963. (18) Raisbeck et al. 1973. (19) Olson et al. 1983. (20) Yiou 1968. (21) "Webber et al. 1998a. (22) Chen et al. 1997b. (23) Knott et al. 1997. (24) Chen et al. 1997a. (25) Schiekel et al. 1996b.

TABLE 7

PARAMETERS FOR ^{9}Be AND ^{10}Be PRODUCTION CROSS SECTION FORMULAE[a]

Parent	Daughter Isotope	σ_0 (mbarn)	ξ	E_0 (MeV nucleon^{-1})
^{11}B	^{9}Be	6.92	...	...
	^{10}Be	5.05	...	...
^{12}C	^{9}Be	5.76	0.185	2545
	^{10}Be	3.79	0.530	1037
^{13}C	^{9}Be	6.61	...	...
	^{10}Be	5.60	...	...
^{14}N.....	^{10}Be	1.75	0.715	671
^{16}O.....	^{9}Be	4.04	0.558	637
	^{10}Be	2.52	0.962	798

[a] See eq. (B1).

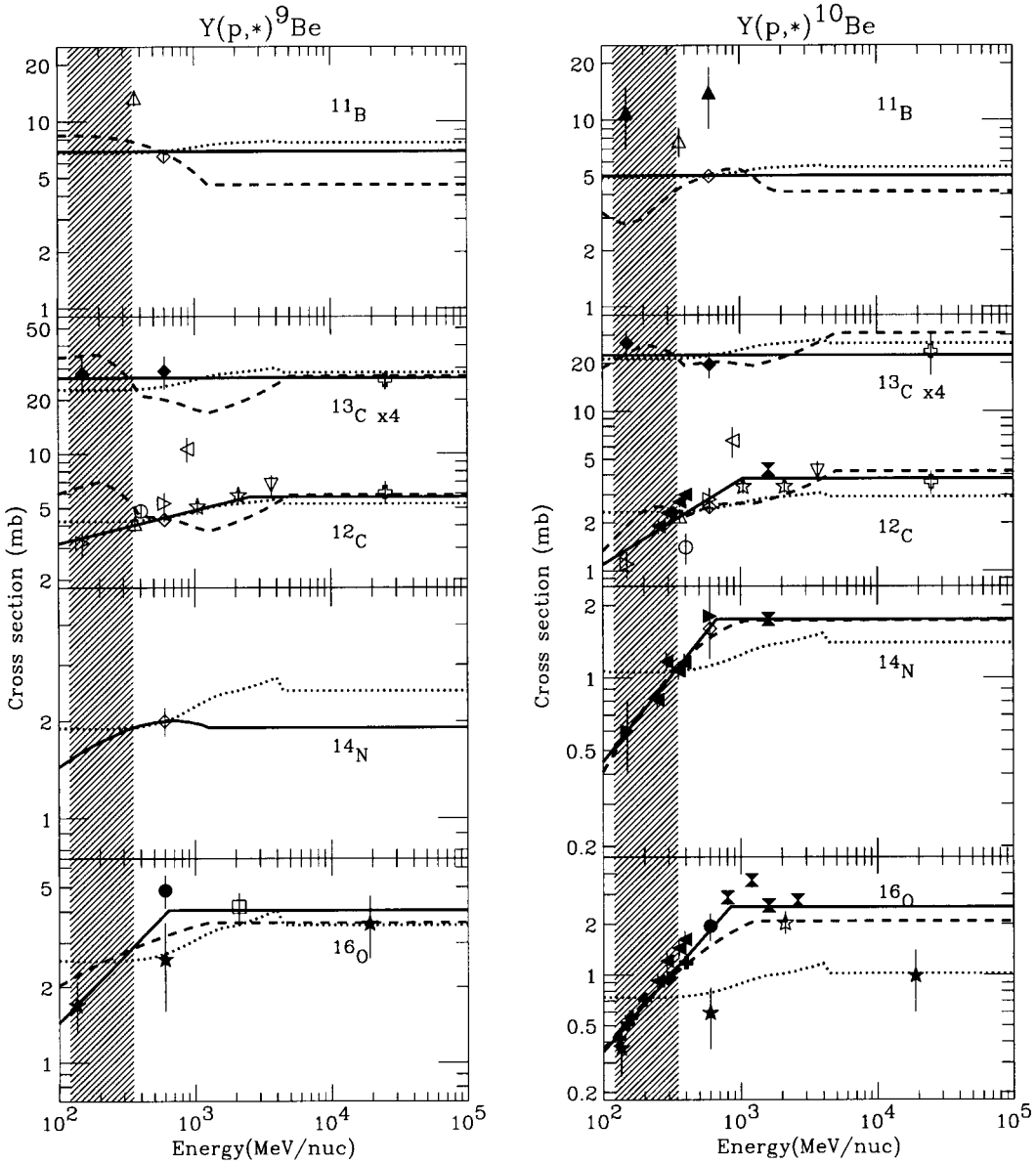

FIG. 11.—Partial fragmentation cross section data for the production of Be isotopes from a parent species "Y" and predictions from the formulae of STB and WKS, normalized to the data. Curves from STB are shown as dashed lines, and curves from WKS are shown as dotted lines. The solid curves are functions used in this study, fitted to the form in eq. (B1). The isotope names labeling the curves are the parent species "Y" that produce the Be isotopes. In the case of the cross section for the production of ^{9}Be from ^{14}N, the prediction from STB is used in this study, so the solid curve is shown overlying the dashed curve in this panel. The hatched band corresponds to the approximate ISM energy range appropriate to the CRIS data for Be. References for the cross section data are as follows: *Open diamond*, Webber, Kish, & Schrier (1990a); *open square*, Olson et al. 1983; *open upward triangle*, Webber et al. (1998b); *open star*, Lindstrom et al. (1975); *open downward triangle*, Korejwo et al. (1999); *open circle*, Webber & Kish (1985); *open right triangle*, Fontes et al. (1971); *open left triangle*, Lestringuez et al. (1971); *open plus sign*, Yiou et al. (1973); *filled diamond*, Raisbeck, Lestringuez, & Yiou (1973); *filled upward triangle*, Raisbeck & Yiou (1976); *filled star*, Yiou (1968); *filled circle*, Raisbeck & Yiou (1977); *filled right triangle*, Raisbeck & Yiou (1974); *filled left triangle*, Schiekel et al. (1996a); *filled hourglass*, Michel et al. (1995); *filled plus sign*, Sisterson et al. (1997).

adopt the formulae from either group for the production of ^{10}Be, we used a constant value for parent reactions with few measurements and matched a power law at low energies to a constant value at high energies for reactions having multiple measurements. That is, the production cross sections for ^{9}Be and ^{10}Be have the following form:

$$\sigma_{i,\mathrm{Be}}(E) = \sigma_0\left(\frac{E}{E_0}\right)^{\xi}, \qquad \text{where } \xi = 0 \text{ for } E \geq E_0\,. \tag{B1}$$

Coefficients from the weighted least-squares fit for this form are listed in Table 7, and the fits are plotted in Figure 11 as solid curves. The term E_0 was determined as the crossover point after fitting data below 3 GeV nucleon^{-1} to a power law and data above 1 GeV nucleon^{-1} to a constant value. Figure 12 shows the similar cross section comparisons for production of the isotopes of Al.

After normalizing the energy dependences of WKS and STB to cross section data at energies appropriate to this study, the mean path length is virtually identical for the low-Z secondary-to-primary ratios using the WKS or STB energy dependence,

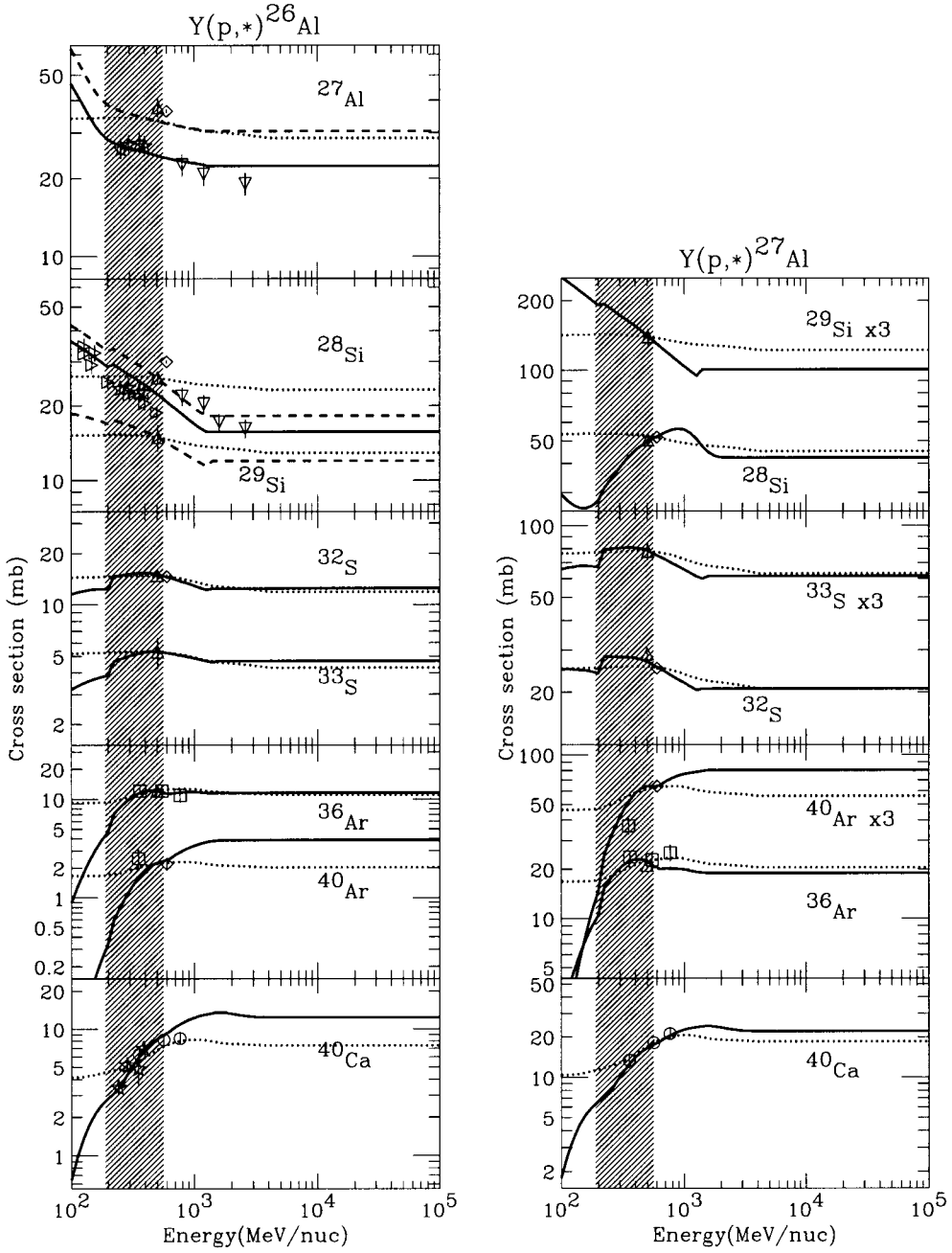

FIG. 12.—Partial fragmentation cross section data for the production of Al isotopes from a parent species "Y" and predictions from the formulae of STB and WKS, normalized to the data. Curves from STB are shown as dashed lines, and curves from WKS are shown as dotted lines. The solid curves are the STB predictions used in this study, which overlie the dashed lines for all panels except in the cases of the production of ^{26}Al from ^{27}Al or ^{28}Si. In these cases, data from Webber et al. (1990a) and Webber et al. (1998a) disagree significantly with measurements from other experiments, and the solid curves do not include the Webber et al. (1990a, 1998a) data in the normalization of the curves to data. The isotope names labeling the curves are the parent species "Y" that produce the Al isotopes. The hatched region corresponds to the approximate ISM energy range appropriate to the CRIS data for Al. References for the cross section data are as follows: *Open diamond*, Webber et al. (1990a); *open square*, Knott et al. (1997); *open circle*, Chen et al. (1997a); *open upward triangle*, Webber et al. (1998a); *open star*, Schiekel et al. (1996a); *open downward triangle*, Michel et al. (1995); *open right triangle*, Sisterson et al. (1997).

but the WKS path length for the Fe-group is 65% higher than the STB value. Figure 13 compares the values of the clock isotope ratios calculated assuming various values of the ISM hydrogen density using the different cross section formulae. The CRIS measurements of the abundance ratios are also shown for comparison. For both Be and Al the cross section formulae tend to agree best around a few hundred MeV nucleon^{-1}, where they are best constrained by measurements. In this region, the predicted value of the ISM density is more reliable because it depends more directly on the cross section measurements.

At the lowest energies for Be that were measured by CRIS, differences among STB, WKS, and the energy dependence used in this study are large because the most statistically significant cross section measurements were made at energies considerably higher than the ISM energy relevant to the CRIS data. One can compare results derived using the energy dependences from STB and WKS to the fits used in this study to gain some insight about the amount of uncertainty attributable to theoretical cross section predictions. The average difference among values based on ^{10}Be shown in Figure 13 is $\Delta n_{\rm H} \sim \pm 10\%$ around an average of $n_{\rm H} = 0.3$ H atoms cm^{-3}. For the lowest energy data points for other species, the uncertainties in Figure

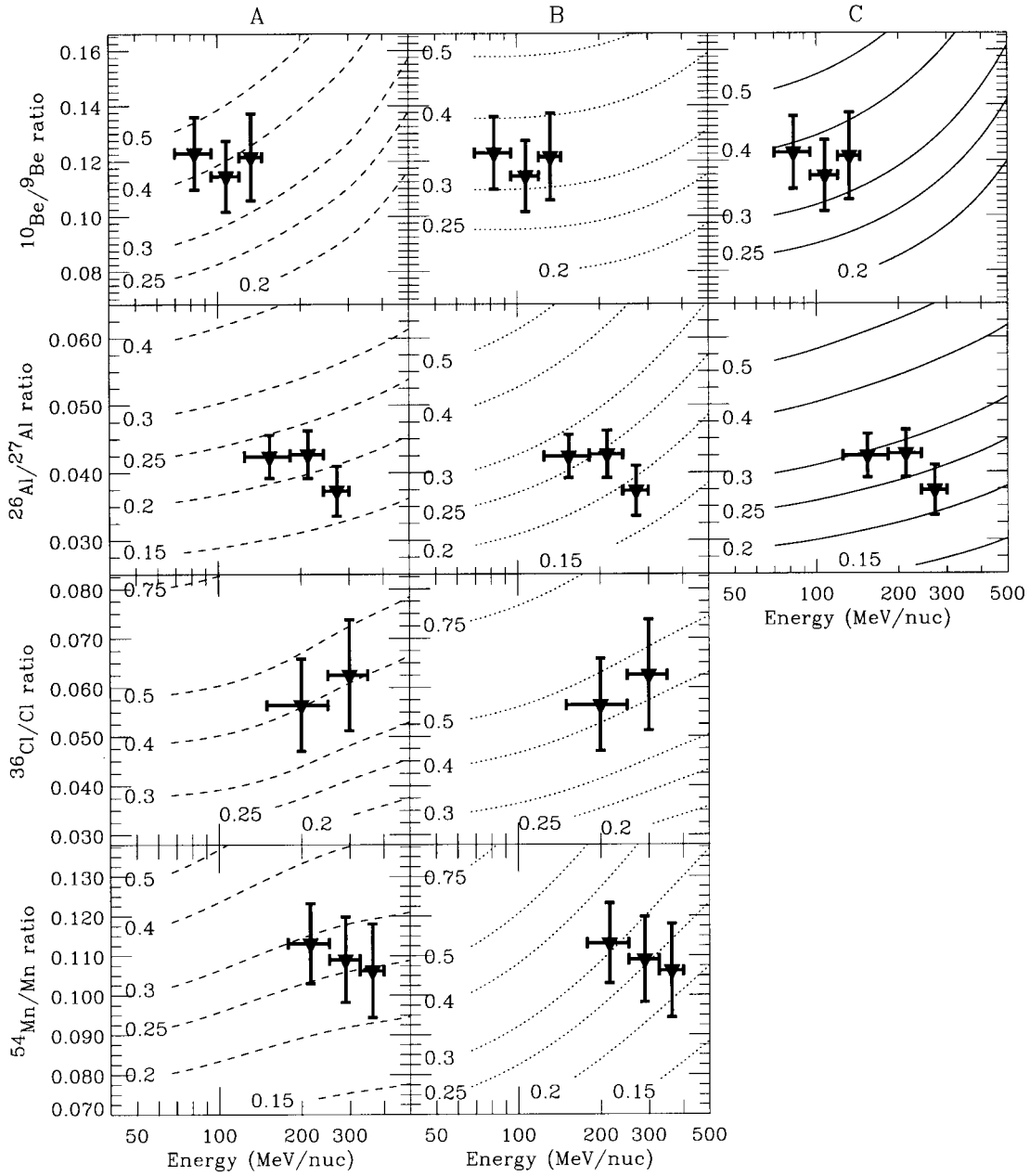

FIG. 13.—Comparison of calculated secondary radioactive-isotope abundance ratios using different formulae for the calculation of production cross sections. The points show the measured CRIS values. The curves are parameterized by the ISM hydrogen density in H atoms cm^{-3}. The dashed curves in column A result from using the semiempirical isotopic fragmentation cross sections formulated by STB, and the dotted curves in column B use the parametric isotopic fragmentation cross section formulation of WKS. For ^{36}Cl/Cl and ^{54}Mn/Mn, the dashed STB curves in column A were used in this study. The solid curves in column C result from the cross sections used in this study for ^{10}Be/^{9}Be and ^{26}Al/^{27}Al. In the case of ^{10}Be/^{9}Be, the cross section fit described in this study and shown in Fig. 11 was used. For ^{26}Al/^{27}Al, data from Webber et al. (1990a, 1998a) were not used in normalizing the cross section curves to experimental measurements as shown in Fig. 12. All three families of curves assume a solar modulation level of $\phi = 325$ MV.

13 are $\Delta n_{\rm H} \sim \pm 7\%$ for ^{26}Al, $\Delta n_{\rm H} \sim \pm 3\%$ for ^{36}Cl, and $\Delta n_{\rm H} \sim \pm 9\%$ for ^{54}Mn. For all species with the exception of ^{36}Cl, these systematic uncertainties are comparable to the statistical uncertainty of the data as reported over the full energy interval. Additional cross section measurements, especially for parent species that contribute $\gtrsim 5\%$–10% of one or more of the clock isotopes, could help to reduce the uncertainties in the derived values of $n_{\rm H}$ and test for significant differences among the values derived from the different radionuclides.

REFERENCES

Ahlen, S. P., et al. 2000, ApJ, 534, 757
Ajzenberg-Selove, F. 1988, Nucl. Phys. A, 490, 1
Anders, E., & Grevesse, N. 1989, Geochim. Cosmochim. Acta, 53, 197
Badhwar, G. D., & O'Neill, P. M. 1993, Proc. 23d Int. Cosmic-Ray Conf. (Calgary), 3, 535
Be, M.-M., Coursol, N., & Duchemin, B. 1999, Table de Radionucléides (Gif-sur-Yvette: Commissariat à l'Energie Atomique)
Binns, W. R. et al. 2000, in AIP Conf. Proc. 528, Acceleration and Transport of Energetic Particles Observed in the Heliosphere: ACE 2000 Symposium, ed. R. Mewaldt, J. Jokipii, M. Lee, E. Mobius, & T. Zurbuchen (Melville: AIP), 413
Buffington, A., Orth, C. D., & Mast, T. S. 1978, ApJ, 226, 355
Chen, C.-X., et al. 1997a, Phys. Rev. C, 56, 1536
———. 1997b, ApJ, 479, 504
Churchwell, E., Mezger, P. G., & Huchtmeier, W. 1974, A&A, 32, 283
Connell, J. J. 1998, ApJ, 501, L59
Connell, J. J., DuVernois, M. A., & Simpson, J. A. 1998, ApJ, 509, L97
Cumming, J. P. 1963, Ann. Rev. Nucl. Sci., 13, 261
Dame, T. M., et al. 1987, ApJ, 322, 706
Davis, A. J., et al. 2000, in AIP Conf. Proc. 528, Acceleration and Transport of Energetic Particles Observed in the Heliosphere: ACE 2000 Symposium, ed. R. Mewaldt, J. Jokipii, M. Lee, E. Mobius, & T. Zurbuchen (Melville: AIP), 421
Davis, L. 1960, Proc. 6th Int. Cosmic-Ray Conf. (Moscow), 3, 220
Diplas, A., & Savage, B. D. 1994, ApJ, 427, 274
DuVernois, M. A. 1997, ApJ, 481, 241
DuVernois, M. A., Simpson, J. A., & Thayer, M. R. 1996, A&A, 316, 555
DuVernois, M. A., & Thayer, M. R. 1996, ApJ, 465, 982
Endt, P. M. 1990, Nucl. Phys. A, 521, 1
Engelmann, J. J., et al. 1990, A&A, 233, 96
Ferrando, P., Lal, N., McDonald, F. B., & Webber, W. R. 1991, A&A, 247, 163
Fichtel, C. E., & Reames, D. V. 1968, Phys. Rev., 175, 1564
Firestone, R. B. 1996, in Table of Isotopes, ed. R. B. Firestone & V. S. Shirley (8th ed.; New York: Wiley), 228
Fisk, L. A. 1971, JGR, 76, 221
Fontes, P., Perron, C., Lestringuez, J., Yiou, F., & Bernas, R. 1971, Nucl. Phys. A, 165, 405
Frisch, P. C. 1998, Space Sci. Rev., 86, 107
Garcia-Munoz, M., Mason, G. M., & Simpson, J. A. 1975, ApJ, 201, L141
Garcia-Munoz, M., Simpson, J. A., Guzik, T. G., Wefel, J. P., & Margolis, S. H. 1987, ApJS, 64, 269
Garcia-Munoz, M., Simpson, J. A., & Wefel, J. P. 1981, Proc. 17th Int. Cosmic-Ray Conf. (Paris), 2, 72
Geier, S. 2000, Ph.D. thesis, Univ. Maryland
Gleeson, L. J., & Axford, W. I. 1968, ApJ, 154, 1011
Goulding, F. S., & Harvey, B. G. 1975, Ann. Rev. Nucl. Sci., 25, 167
Grevesse, N., Noels, A., & Sauval, A. J. 1996, in ASP Conf. Ser. 99, Cosmic Abundances, ed. S. S. Holt & G. Sonneborn (San Francisco: ASP), 117
Hagen, F. A., Fisher, A. J., & Ormes, J. F. 1977, ApJ, 212, 262
Harding, D. S., & Harding, A. K. 1982, ApJ, 257, 603
Jones, F. C. 1979, ApJ, 229, 747
Kibedi, T., et al. 1997, ApJ, 489, 951
Knott, C. N., et al. 1997, Phys. Rev. C, 56, 398
Korejwo, A., Giller, M., Dzikowski, T., Wdowczyk, J., Perelygin, V. V., & Zarubin, A. V. 1999, Proc. 26th Int. Cosmic-Ray Conf. (Salt Lake City), 4, 267
Krombel, K. E., & Wiedenbeck, M. E. 1988, ApJ, 328, 940
Lestringuez, J., Raisbeck, G. M., Yiou, F., & Bernas, R. 1971, Phys. Lett. B, 36, 331
Letaw, J. R., Silberberg, R., & Tsao, C. H. 1983, ApJS, 51, 271
Lindstrom, P. J., Greiner, D. E., Heckman, H. H., Cork, B., & Bieser, F. S. 1975, Document LBL-3650, Lawrence Berkeley Laboratory
Lukasiak, A., Ferrando, P., McDonald, F. B., & Webber, W. R. 1994a, ApJ, 423, 426
Lukasiak, A., McDonald, F. B., & Webber, W. R. 1994b, ApJ, 430, L69
———. 1997a, Proc. 25th Int. Cosmic-Ray Conf. (Durban), 3, 389
———. 1997b, ApJ, 488, 454
Martinez-Pinedo, G., & Vogel, P. 1998, Phys. Rev. Lett., 81, 281
Meneguzzi, M., Audouze, J., & Reeves, H. 1971, A&A, 15, 337
Mewaldt, R. A. 1988, in AIP Conf. Proc. 183, Cosmic Abundances of Matter, ed. C. Waddington (Melville: AIP), 124
Meyer, J. P. 1985, ApJS, 57, 173
Meyer, J. P., Drury, L. C., & Ellison, D. C. 1997, ApJ, 487, 182
Michel, R., et al. 1995, Nucl. Instrum. Methods Phys. Res. B, 103, 183
Nordgren, T. E., Cordes, J. M., & Terzian, Y. 1992, AJ, 104, 1465
Olson, D. L., Berman, B. L., Greiner, D. E., Heckman, H. H., Lindstrom, P. J., & Crawford, H. J. 1983, Phys. Rev. C, 28, 1602
Paresce, F. 1984, AJ, 89, 1022
Peimbert, M. 1975, ARA&A, 13, 113
Perron, C. 1976, Phys. Rev. C, 14, 1108
Ptuskin, V. S., Jones, F. C., & Ormes, J. F. 1996, ApJ, 465, 972
Ptuskin, V. S., & Soutoul, A. 1990, A&A, 237, 445
———. 1998a, A&A, 337, 859
———. 1998b, Space Sci. Rev., 86, 225
Ptuskin, V. S., Soutoul, A., & Streitmatter, R. E. 1999, Proc. 26th Int. Cosmic-Ray Conf. (Salt Lake City), 4, 195
Ptuskin, V. S., Volk, H. J., Zirakshvili, V. N., & Breitschwerdt, D. 1997, A&A, 321, 434
Raisbeck, G. M., Lestringuez, J., & Yiou, F. 1973, Nature Phys. Sci., 244, 28
Raisbeck, G. M., & Yiou, F. 1974, Phys. Rev. C, 9, 1385
———. 1975, Phys. Rev. Lett., 35, 155
———. 1976, in Spallation Nuclear Reactions and Their Applications, ed. B. S. P. Shen & M. Merker (Dordrecht: Reidel), 83
———. 1977, Proc. 15th Int. Cosmic-Ray Conf. (Plovdiv), 2, 203
Schiekel, T., et al. 1996a, Nucl. Instrum. Methods Phys. Res. B, 114, 91
Schiekel, T., Sudbrock, F., Herpers, U., Gloris, M., Leya, I., Michel, R., Synal, H.-A., & Suter, M. 1996b, Nucl. Instrum. Methods Phys. Res. B, 113, 484
Silberberg, R., Tsao, C. H., & Barghouty, A. F. 1998, ApJ, 501, 911 (STB)
Simon, M., & Molnar, A. 1999, Proc. 26th Int. Cosmic-Ray Conf. (Salt Lake City), 4, 211
Simpson, J. A., & Connell, J. J. 1998, ApJ, 497, L85
Simpson, J. A., & Garcia-Munoz, M. 1988, Space Sci. Rev., 46, 205
Sisterson, J. M., et al. 1997, Nucl. Instrum. Methods Phys. Res. B, 123, 324
Soutoul, A., Ferranno, P., & Webber, W. R. 1987, Proc. 21st Int. Cosmic-Ray Conf. (Adelaide), 3, 337
Soutoul, A., & Ptuskin, V. S. 1999, Proc. 26th Int. Cosmic-Ray Conf. (Salt Lake City), 4, 184
Stephens, S. A., & Streitmatter, R. E. 1998, ApJ, 505, 266
Streitmatter, R. E., et al. 1993, Proc. 23d Int. Cosmic-Ray Conf. (Calgary), 2, 623
Stone, E. C., et al. 1998a, Space Sci. Rev., 86, 285
———. 1998b, Space Sci. Rev., 86, 357
Strong, A. W., & Moskalenko, I. V. 1998, ApJ, 509, 212
———. 1999, Proc. 26th Int. Cosmic-Ray Conf. (Salt Lake City), 4, 255
Tan, L. C., Mason, G. M., Gloeckler, G., & Ipavitch, F. M. 1987, Proc. 20th Int. Cosmic-Ray Conf. (Moscow), 2, 239
Taylor, J. H., & Cordes, J. M. 1993, ApJ, 411, 674
Webber, W. R. 1982, ApJ, 252, 386
———. 1993, ApJ, 402, 188
Webber, W. R., & Kish, J. C. 1979, Proc. 16th Int. Cosmic-Ray Conf. (Kyoto), 1, 389
———. 1985, Proc. 19th Int. Cosmic-Ray Conf. (La Jolla), 3, 87
Webber, W. R., Kish, J. C., Rockstroh, Y., Cassagnou, Y., Legrain, R., Soutoul, A., & Testard, O. 1998a, Phys. Rev. C, 58, 1
Webber, W. R., Kish, J. C., Rockstroh, Y., Cassagnou, Y., Legrain, R., Soutoul, A., Testard, O., & Tull, C. 1998b, ApJ, 508, 949
Webber, W. R., Kish, J. C., & Schrier, D. A. 1990a, Phys. Rev. C, 41, 547
———. 1990b, Phys. Rev. C, 41, 566 (WKS)
Webber, W. R., Lezniak, J. A., Kish, J. C., & Simpson, G. A. 1977, Astrophys. Lett., 18, 125
Westfall, G. D., Wilson, L. W., Lindstrom, P. J., Crawford, H. J., Greiner, D. E., & Heckman, H. H. 1979, Phys. Rev. C, 19, 1309
Wiedenbeck, M. E. 1983, Proc. 18th Int. Cosmic-Ray Conf. (Bangalore), 9, 147
Wiedenbeck, M. E., et al. 2000, in AIP Conf. Proc. 528, Acceleration and Transport of Energetic Particles Observed in the Heliosphere: ACE 2000 Symposium, ed. R. Mewaldt, J. Jokipii, M. Lee, E. Mobius, & T. Zurbuchen (Melville: AIP), 363
Wiedenbeck, M. E., & Greiner, D. E. 1980, ApJ, 239, L139
Wuosmaa, A. H., et al. 1998, Phys. Rev. Lett., 80, 2085
Yanasak, N. E., et al. 1999, Proc. 26th Int. Cosmic-Ray Conf. (Salt Lake City), 3, 9 (Y1999)
———. 2000, in AIP Conf. Proc. 528, Acceleration and Transport of Energetic Particles Observed in the Heliosphere: ACE 2000 Symposium, ed. R. Mewaldt, J. Jokipii, M. Lee, E. Mobius, & T. Zurbuchen (Melville: AIP), 402 (Y2000)
Yiou, F. 1968, Ann. Phys., 3, 169
Yiou, F., Raisbeck, G., Perron, C., & Fontes, P. 1973, Proc. 13th Int. Cosmic-Ray Conf. (Denver), 1, 512
Zaerpoor, K., et al. 1997, Phys. Rev. Lett., 79, 4306
———. 1999, Phys. Rev. Lett., 82, 2219